Diffracted wave-field decomposition and multi-dimensional site effects in the Argostoli valley, Greece

Afifa Imtiaz, C Cornou, Pierre-Yves Bard, M Hobiger

Geophysical Journal International

Geophys. J. Int. (2021) **224,** 1849–1869
Advance Access publication 2020 November 05
GJI Seismology

doi: 10.1093/gji/ggaa529

Diffracted wavefield decomposition and multidimensional site effects in the Argostoli valley, Greece

A. Imtiaz [1,2] C. Cornou,[3] P.-Y. Bard[3] and M. Hobiger[2]

[1] *BRGM, F*-45060 *Orléans, France. E-mail: afifa.imtiaz@sed.ethz.ch*
[2] *Swiss Seismological Service, ETH Zurich, CH*-80192 *Zurich, Switzerland*
[3] *Univ. Grenoble Alpes, Univ. Savoie Mont-Blanc, CNRS, IRD, UGE, ISTerre,* 38058 *Grenoble Cedex* 9, *France*

Accepted 2020 November 3. Received 2020 September 10; in original form 2020 March 24

SUMMARY

Effects of seismic ground motion induced by surface geology and geometry are known to be associated with the generation of a substantial proportion of surface waves. As a consequence, surface waves significantly contribute to ground-motion variability and site amplification. There is a growing body of literature recognizing that an understanding of physical patterns of the wavefield crossing a site is the key aspect to characterize and quantify them. However, this task remains technically challenging due to the complexity of such effects as well as the limitations of geophysical investigations, especially in case of small sedimentary valleys. The present study attempts to investigate the waves propagating across two 2-D dense seismic arrays from a number of earthquakes and explore the extent to which they are contributing to the multidimensional site effects. The arrays were deployed in the small-size, shallow alluvial valley of Koutavos-Argostoli, located in Cephalonia Island, Greece, and consisted of three-component velocimeters with interstation distances ranging from 5 to 160 m. A set of 46 earthquakes, with magnitudes between 2 and 5 and epicentral distances up to 200 km, was analysed by using an advanced seismic array processing technique, MUSIQUE. The phase velocity, backazimuth and energy of the dominant waves crossing the array were extracted, and their identification as Love or prograde/retrograde Rayleigh waves was obtained. The results clearly indicate a predominance of scattered surface waves (up to 60 per cent of total energy), mainly from the closest valley edges, above the fundamental frequency ($\sim$1.5 Hz) of the valley. Love waves dominate the low-frequency wavefield ($<$3 Hz) while Rayleigh waves dominate some high-frequency bands. An excellent consistency is observed, in a given frequency range, among the dominance of the type of diffracted surface waves, group velocities estimated from the ground velocity structure and site amplification. The outcomes of this research provide a better understanding of the contribution of edge-diffracted surface waves and the 2-D/3-D site amplification at small and shallow alluvium valleys like Argostoli. The method applied here can be used to calibrate and validate 3-D models for simulating seismic ground motion.

Key words: Time-series analysis; Earthquake ground motions; Site effects; Wave propagation; Wave scattering and diffraction.

1 INTRODUCTION

Site-specific characteristics of ground motions are important for the estimation of seismic design parameters in engineering applications. Seismological observations have indicated that effects of surface geology and geometry (e.g. sedimentary valleys, topography) significantly contribute to the ground-motion amplification and variability. Hence, they are strongly correlated with earthquake damage, as witnessed by most of the past destructive earthquakes (e.g. Mexico City 1985; Loma Prieta 1989; Kobe 1995; Izmit 1999; Puebla 2017). Although it was initially believed that body waves trapped in sedimentary layers are mainly responsible for the amplification of ground motion, the contribution of locally generated surface waves is now widely recognized (e.g. Kawase 1996). Especially, surface waves diffracted by basin edges significantly modify the wavefield and the resulting ground motion, leading to large amplifications, duration lengthening, and significant ground strains (Moczo & Bard 1993; Field 1996; Chávez-García *et al.* 1999; Cornou *et al.* 2003a,b; Bindi *et al.* 2009; Scandella & Paolucci 2010). Such motions can substantially increase seismic forces on structures and lifelines, particularly in small sedimentary valleys where edge-induced waves reverberate within shallow layers and contribute to the generation

of trapped surface waves in the presence of 2-D or 3-D local heterogeneities. These short-period surface waves appear early in the seismogram and blend into the direct shear- (*S*-) wave train. Complexity of such wavefields makes the distinction between body and surface waves an intricate task.

In the existing literature, most of the observations addressing the presence of locally generated surface waves concern long-period (i.e. low-frequency) waves, propagating in large and deep basins. Most numerical studies in this regard do not cover the broad frequency range of engineering interest (0.5–20 Hz); they are rather limited to frequencies below 2 Hz. The issue of complex mixing of surface waves in small sedimentary valleys was addressed in literature (e.g. Caserta *et al.* 1998; Gaffet *et al.* 1998; Chávez-García *et al.* 1999; Rovelli *et al.* 2001; Cornou *et al.* 2003a,b; Bindi *et al.* 2009), where the authors have analysed dense array data to characterize the seismic wavefield. However, most of them derive site effects from the 1-D modelling approaches and do not account for the influence of different types of surface waves. Thus more sophisticated studies, in view of a better understanding of complex wavefields and site effects, are required to improve the routine seismic hazard assessment of urban areas on sedimentary basins.

This paper is an attempt to address the issue of characterizing locally generated surface waves and their contribution to site effects at a small sedimentary valley. We analyse seismic data recorded by two dense arrays in the Koutavos-Argostoli valley located on the island of Cephalonia, Greece. Among various available array-processing techniques, we applied the MUSIQUE algorithm (Hobiger *et al.* 2012, 2016) in order to extract the wavefield parameters (backazimuth and slowness) and identify the contributions of Love and Rayleigh waves. We start this paper with a brief overview of the principle of seismic wavefield analysis. Then we present the site, arrays and the data set. We provide a brief description of the MUSIQUE technique and elaborate the data-analysis steps. Finally, we discuss the results with respect to possible physical implications.

2 METHODOLOGY

2.1 Seismic wavefield analysis

Two types of seismic body waves, *P* (primary or compressional) and *S* (secondary or shear), exist in elastic media. *P*-wave motion is longitudinal and *S*-wave motion is transverse to the direction of their propagation. Two different types of *S* waves (*SH* and *SV*) are further defined with respect to their plane of polarization. The polarization of *SH* waves lies in a horizontal plane and that of *SV* waves in vertical. In a homogeneous medium, both *P* and *S* waves travel at their respective velocities at all frequencies. However, the underground structure of the Earth consists of different layers with different material properties. The complex propagation of body waves through the interfaces of these layers gives rise to the surface waves. As they travel close to the surface of the Earth and are sensitive to different depth ranges depending on their wavelengths, surface waves are particularly suited for exploring the local, shallow undergrounds. There are two main types of surface waves, known as Love and Rayleigh waves. Love waves result from *SH* waves trapped in a shallow, layered subsurface. Their motion is parallel to the surface and they travel with different velocities at different frequencies. The coupled propagation of interfering *P* and *SV* waves results in Rayleigh waves. Their particle motion is elliptical. For a layered structure, Rayleigh waves are dispersive and the ellipticity varies with frequency. Hence, the wave motion can be prograde or retrograde at different frequencies.

While travelling through a heterogeneous underground structure, where the shear wave velocity (V_s) varies with depth, surface waves demonstrate a dispersive behaviour. This means that the phase velocity (v) of a surface wave, at which a peak or a trough propagates, is a function of frequency (f). For a regular ground velocity model (V_s increasing with depth), low-frequency surface waves with larger wavelengths ($\lambda = v/f$) sample deeper layers, where the V_s is generally larger. As a result, they travel faster than high-frequency surface waves, which sample relatively low-velocity, superficial layers. Surface waves traveling at a given velocity can also propagate in several modes, each possessing a unique phase velocity for each wavelength. The mode associated with the lowest phase velocity is defined as the fundamental mode and the others are referred to as higher modes. For any given mode, the depth of influence is proportional to the wavelength.

The estimation of the V_s profile (V_s versus depth) is important for ground-motion amplification and site response studies in sedimentary basins. Dispersion curves (phase velocity as a function of frequency) retrieved from the analysis of surface waves directly depend on the shear wave velocity profile of the soil and can be inverted to constrain the local underground structure. In general, the fundamental mode dominates the wavefield and is used to estimate V_s profiles. Higher modes provide additional constraints and improve the V_s estimates in case of complex profiles (Casto *et al.* 2010). In addition, polarization properties (retrograde or prograde particle motion) of Rayleigh waves provide useful information about different seismic phases (Fäh *et al.* 2003; Poggi & Fäh 2010; Hobiger *et al.* 2013; Maranò *et al.* 2017).

The propagation of a plane seismic wave in terms of its direction and velocity is generally described by the wavenumber vector (k). Arrays of seismic stations offer a handy solution to retrieve it from the analysis of recorded earthquakes. The basic principle of any array analysis technique involves measuring arrival time delays of an incident wave recorded at different stations and estimating its slowness ($s = 1/v$) and backazimuth (θ); here, θ at a given station is defined as the angle measured clockwise from the north to the direction of seismic wave arrival. Hence, array analysis helps us to determine the dispersive nature as well as the scattering of surface waves in a complex wavefield. However, this complexity cannot be identified in seismograms of single stations or a 1-D seismic array. Moreover, records from all three components (3C) of the seismic stations are essential for estimating polarization properties of the waves. Such 3C seismic data from 2-D arrays were successfully used for the analysis of complex wavefields in many previous studies (Jurkevics 1988; Dainty & Toksöz 1990; Wagner & Owens 1993; Kuwahara *et al.* 1997; Bear *et al.* 1999; Cornou *et al.* 2003a,b; Poggi & Fäh 2010; Hobiger *et al.* 2012; Maranò *et al.* 2012, 2017).

Various signal processing techniques exist to process the data from dense seismic arrays. Three commonly used methods in seismology are conventional frequency–wavenumber or FK (Lacoss *et al.* 1969), high-resolution frequency–wavenumber or HRFK (Capon 1969), and Multiple Signal Characterization or MUSIC (Schmidt 1981, 1986). Comparative studies (Goldstein & Archuleta 1987, 1991; Krim & Viberg 1996; Zerva & Zhang 1996; Bokelmann & Baisch 1999; Almendros *et al.* 2000; Cornou *et al.* 2003a; Roullé & Chávez García 2005) among these methods suggested that MUSIC has better resolving power than FK and HRFK in the case of multiple, closely spaced arrivals, and is able to handle

difficult scenarios involving highly correlated waves (containing same frequency contents and phases but arriving from different directions at the same time). Goldstein & Archuleta (1987) showed that MUSIC is particularly well-suited for seismic array analysis because (1) it has the ability to resolve multiple, closely spaced sources, (2) it works with both stationary and non-stationary signals, (3) it is more sensitive to the strongest sources and (4) it provides a unique solution to the wavenumber estimation problem. Roullé & Chávez García (2005) concluded that MUSIC is more useful in case of data with high coherence and small time delays.

2.2 MUSIQUE algorithm

Keeping the advantages of MUSIC in mind, we have chosen an advanced version of this algorithm, known as MUSIQUE (Hobiger *et al.* 2012, 2016), to analyse the dense seismic array data in the present study. MUSIQUE combines the original MUSIC algorithm (Schmidt 1981, 1986, Goldstein & Archuleta 1987) with the quaternion-MUSIC (Miron *et al.* 2005, 2006) in order to resolve the wave vector and to identify the types of surface waves. For a more detailed description of the MUSIQUE algorithm, we refer interested readers to Hobiger *et al.* (2011), who presented its application on synthetic seismic data and showed its potential in identifying Love and Rayleigh waves as well as in separating Rayleigh wave polarizations. Hobiger *et al.* (2016) and Manea *et al.* (2017) used MUSIQUE to analyse earthquake records from the Santa Clara valley in California, USA, and from Bucharest, Romania, respectively. They showed that this algorithm is capable of separating the contributions of Love and Rayleigh waves along with providing the propagation characteristics of the dominant waves. The principle of this technique is briefly presented in the following paragraphs.

The MUSIQUE algorithm first retrieves the slowness (or phase velocity) and backazimuth of the dominant waves crossing the array with "classical" MUSIC, which is based on the separation of signal and noise subspace followed by an estimation of the signal parameters from the eigenstructure of the covariance matrix. Let us assume a data set recorded by an array of N three-component sensors. Then three complex data vectors $X_l(f)$ of size $N \times 1$, can be used to store the data for each frequency (f), where $l = 1, 2, 3$ denote the vertical, east and north components, respectively. The covariance matrix (size $N \times N$) calculated for each component is given by

$$S_l = E\left[X_l(f)\ X_l^*(f)\right], \tag{1}$$

where E denotes the mathematical expectation value and the $*$-operator denotes complex conjugation. The expectation value is realized by averaging $X_l(f)\ X_l^*(f)$ over several neighbouring frequency values, that is, from $f - \Delta$ to $f + \Delta$. The covariance matrix $S(f)$ is derived by simply summing up the covariance matrices of the single components. Subsequently, the eigenvectors and eigenvalues are calculated. The eigenvectors corresponding to the K strongest eigenvalues define the signal subspace ($K < N$), while the $N - K$ weakest eigenvalues define the noise subspace G. Then, from the set of array manifold vectors, the ones that give the minimum projection onto the noise subspace are determined through the search of the maxima of the MUSIC functional expressed as

$$P = \frac{1}{a^H(k)\ GG^H\ a(k)}, \tag{2}$$

where H denotes the conjugate transpose of a matrix. The steering vector a is given as

$$a = \frac{\exp(-i\,\boldsymbol{R}k)}{\sqrt{N}}. \tag{3}$$

It indicates the theoretical phase delays for the different stations of the array located at the sensor positions $\boldsymbol{R}$ for the propagation of a wave with wave vector k, expressed as

$$k = -2\pi f s(f)\ (\sin\theta,\ \cos\theta,\ 0)^T, \tag{4}$$

where θ is the backazimuth and s is the slowness of the wave.

Radial and transverse motions of the waves are determined by projecting the horizontal components of the signal in the backazimuth direction θ, while the vertical component remains unchanged. They are expressed as

$$X_{\text{radial}} = -\sin\theta\ X_2(f) - \cos\theta\ X_3(f), \tag{5}$$

$$X_{\text{transverse}} = \cos\theta\ X_2(f) - \sin\theta\ X_3(f), \tag{6}$$

$$X_{\text{vertical}} = X_1(f). \tag{7}$$

The energies of different components for each station are calculated by

$$E_{\text{vertical}} = \sum_{f=f_c-\Delta}^{f=f_c+\Delta} \vec{X}_1^*(f)\ \vec{X}_1(f), \tag{8}$$

$$E_{\text{east}} = \sum_{f=f_c-\Delta}^{f=f_c+\Delta} \vec{X}_2^*(f)\ \vec{X}_2(f), \tag{9}$$

$$E_{\text{north}} = \sum_{f=f_c-\Delta}^{f=f_c+\Delta} \vec{X}_3^*(f)\ \vec{X}_3(f), \tag{10}$$

$$E_{\text{radial}} = \sin^2\theta\ E_{\text{east}} + \cos^2\theta\ E_{\text{north}} + \sin\theta\ \cos\theta\ E_m, \tag{11}$$

$$E_{\text{transverse}} = \cos^2\theta\ E_{\text{east}} + \sin^2\theta\ E_{\text{north}} - \sin\theta\ \cos\theta\ E_m, \tag{12}$$

where the summation is realized over the same number of frequencies around the target frequency f_c as in eq. (1). To ensure good results, it is sufficient to sum over five frequency values (i.e. $\Delta = 2$). The cross-term, E_m, is calculated as

$$E_m = \sum_{f=f_c-2\Delta}^{f=f_c+2\Delta} \left(\vec{X}_2^*(f)\ \vec{X}_3(f) + \vec{X}_3^*(f)\ \vec{X}_2(f)\right). \tag{13}$$

An energy criterion is then considered to discriminate between Love and Rayleigh waves. If $\boldsymbol{E}_{\text{transverse}} > \boldsymbol{E}_{\text{vertical}} + \boldsymbol{E}_{\text{radial}}$, the wave is identified as a Love wave. In the opposite case, it is considered as a possible Rayleigh wave and its identification is done based on the determination of the polarization parameters by applying quaternion-MUSIC.

By definition, quaternions are considered as an extension of complex numbers into four dimensions (Ward 1997), that is, in addition to the complex unit i there are two more complex units j and k, with $i^2 = j^2 = k^2 = ijk = 1$. Two complex-valued data matrices corresponding to different components can be stored in a single quaternion-valued data matrix. The quaternion-MUSIC algorithm

is used to merge both complex-valued data vectors of the radial and vertical components into a single data matrix so that the phase information and the sense of rotation of the particle motion remain naturally preserved, hence allowing the distinction between retrograde and prograde Rayleigh wave motions. The quaternion-valued data matrix is defined as

$$X_q\ (f) = \mathrm{Re}\,(X_1\,(f)) + i\ \mathrm{Im}\,(X_1\,(f)) + j\ \mathrm{Re}\ (X_{Radial}\,(f)) + k\ \mathrm{Im}\ (X_{\mathrm{Radial}}\,(f))\,. \quad (14)$$

The definition of the quarternion-valued covariance matrix and the quarternion-MUSIC functional are analogue to eqs (1) and (2), respectively. However, the steering vector is expressed as

$$a_q\ (k) = \frac{[\cos\rho + i\sin\rho\ \exp(j\varphi)]\ \exp(-j\,R\boldsymbol{k})}{\sqrt{N}}\,, \quad (15)$$

where ρ is the amplitude parameter describing the ratio between the radial and vertical amplitudes (the ellipticity would then be given by tan ρ) and φ is the phase difference between the vertical and the radial components. In the original quarternion-MUSIC algorithm (Miron *et al.* 2005, 2006), a 4-D grid search leads to the identification of these four wave propagation parameters ($\theta,\ s,\ \varphi,\ \rho$). However, in MUSIQUE, the first two parameters ($\theta,\ s$) are already estimated using the first step (classical MUSIC). The remaining two parameters ($\varphi,\ \rho$) can be determined analytically, which significantly optimizes the calculation time. It is worth mentioning that, even though classical MUSIC is able to identify multiple dominant sources, the MUSIQUE algorithm is limited to a single wave contribution, that is, to the most dominant source ($K = 1$), because it requires projection of the horizontal signals onto the backazimuth for the estimation of polarization parameters.

3 DATA

3.1 Study site

Argostoli is the capital of Cephalonia, one of the central Ionian Islands of Greece. The current study has taken place at the Koutavos-Argostoli site, a relatively small alluvial valley situated on the eastern shore of the Gulf of Argostoli (Fig. 1a). The dense seismic arrays under consideration were deployed at the Koutavos Park, just to the south of the Bay (Fig. 1b). The area is surrounded by the Tilegrafos hills and the city of Argostoli to the west, the coastal plain of Krane to the south and the foothill of the Aenos mountain range to the east.

Cephalonia is located in a complex tectonic environment at the north-westernmost boundary of the Aegean plate. A major right-lateral strike-slip fault system, known as the Cephalonia Transform Fault (CTF), marked by a red line in Fig. 1(a), limits the Island to the west and contributes significantly to the region's geodynamic complexity (Le Pichon *et al.* 1995; Louvari *et al.* 1999). The available geological description of the area demonstrates that the Pre-Apulian zone forms the major part of Cephalonia. This rock unit consists mainly of a thick sequence of carbonates (limestone and dolomite) of Triassic to Middle Miocene age, overlain by a much thinner fine clastic sequence of marl and pelite of Middle Miocene to Lower Pliocene age. According to Lekkas *et al.* (2001), the study area Koutavos-Argostoli is mainly composed of Holocene-Pleistocene alluvial deposits. According to existing literature (Protopapa *et al.* 1998), the valley is about 3 km long and 1.5 km wide, surrounded by hills of limestone and marl, and covered by soft Neogene sediments down to the depth (h) of 40 to 50 m. An updated geological map provided by a more recent study (Hollender *et al.* 2015; Cushing *et al.* 2016, 2020) is presented in (Fig. 1b). It demonstrates that the valley is formed of mainly Plio-Quaternary and Pliocene deposits. Fig. 1(c) shows the horizontal-to-vertical (H/V) spectral ratio calculated from 1 hr of ambient noise recorded by a Güralp CGM6TD acquisition unit at the centre of the valley (marked as (c) in Fig. 1d). The peak exhibited by this curve lies between 1.5 and 2 Hz, which indicates the fundamental frequency of resonance of the site (f_0). The H/V peak frequencies estimated at a number of locations across and along the valley axes show that the average fundamental frequency at the site is around 1.5 Hz (Theodoulidis *et al.* 2018).

3.2 Argostoli dense seismic arrays

The dense seismic arrays considered in this study were deployed in the Koutavos-Argostoli area during the high-resolution seismological experiment undertaken as part of the Network of European Research Infrastructures for Earthquake Risk Assessment and Mitigation (NERA) 2010–2014 project funded by the European Community's (EC) Seventh Framework Program (FP7). They were operational from 2011 September 20 to 2012 April 17. In addition, geophysical and geological surveys (Theodoulidis *et al.* 2018) have been performed on the site to constrain the V_s structure. Fig. 1(b) shows locations of the arrays, called Array A and Array B, on the updated geological map. Fig. 1(d) shows the 2-D southwest–northeast (SW–NE) cross-section of the valley, marking the approximate locations of different features from Fig. 1(b). The two reference stations R01 and R02, about 2 km apart from each other, are situated on relatively softer and stiffer rock sites, respectively. The rock station R02 (Fig. 1 b) has been used as a reference site in this study. It is installed at the northeastern edge on limestones of the upper Cretaceous, in a flat area at the foot of a hill. The H/V calculated at the site shows an amplitude less than 2 and a relatively flat spectrum over the entire frequency range, which is considered to be adequate for a reference station (Theodoulidis *et al.* 2018). The mean of shear wave velocities over the first 30 m depth of the soil (V_{s30}) is considered to be around 670 m s^{-1}. It is assumed to be similar to one measured at a site 2.5 km to the southeast, seated on the same geologic formation (Theodoulidis *et al.* 2018).

Array A consists of 21 broad-band velocimeters (Güralp CMG40T sensors with eigenperiods between 30 and 60 s) connected to Nanometrics Taurus digitizers, with a sampling frequency of 200 Hz. The geometric configuration of the array is provided in Fig. 2(a). All stations are placed on the same geological unit, on four concentric circles with radii of 5, 15, 40 and 80 m, respectively, around the central station A00. Sensors are placed on straight lines at an angle of 39°, 112°, 183°, 255° and 328° with respect to the north direction seen from A00. The minimum and maximum interstation distances of the array are 5 and 153 m, respectively. Such a circular configuration ensures azimuth-independent receiver characteristics over a wide range of wavelengths. Array B consists of 10 short-period velocimeters (Mark L4C-3D sensors with resonance frequency of 1 Hz) with a sampling frequency of 100 Hz. The geometric configuration of the array is provided in Fig. 2(b). The interstation distances for the array range from 5 to 60 m.

Figs 2(c) and (d) present the response functions of Array A and Array B, respectively, in the wavenumber (k) plane. The array response function describes the sensitivity and the theoretical resolution capacity of an array across which signals are propagating

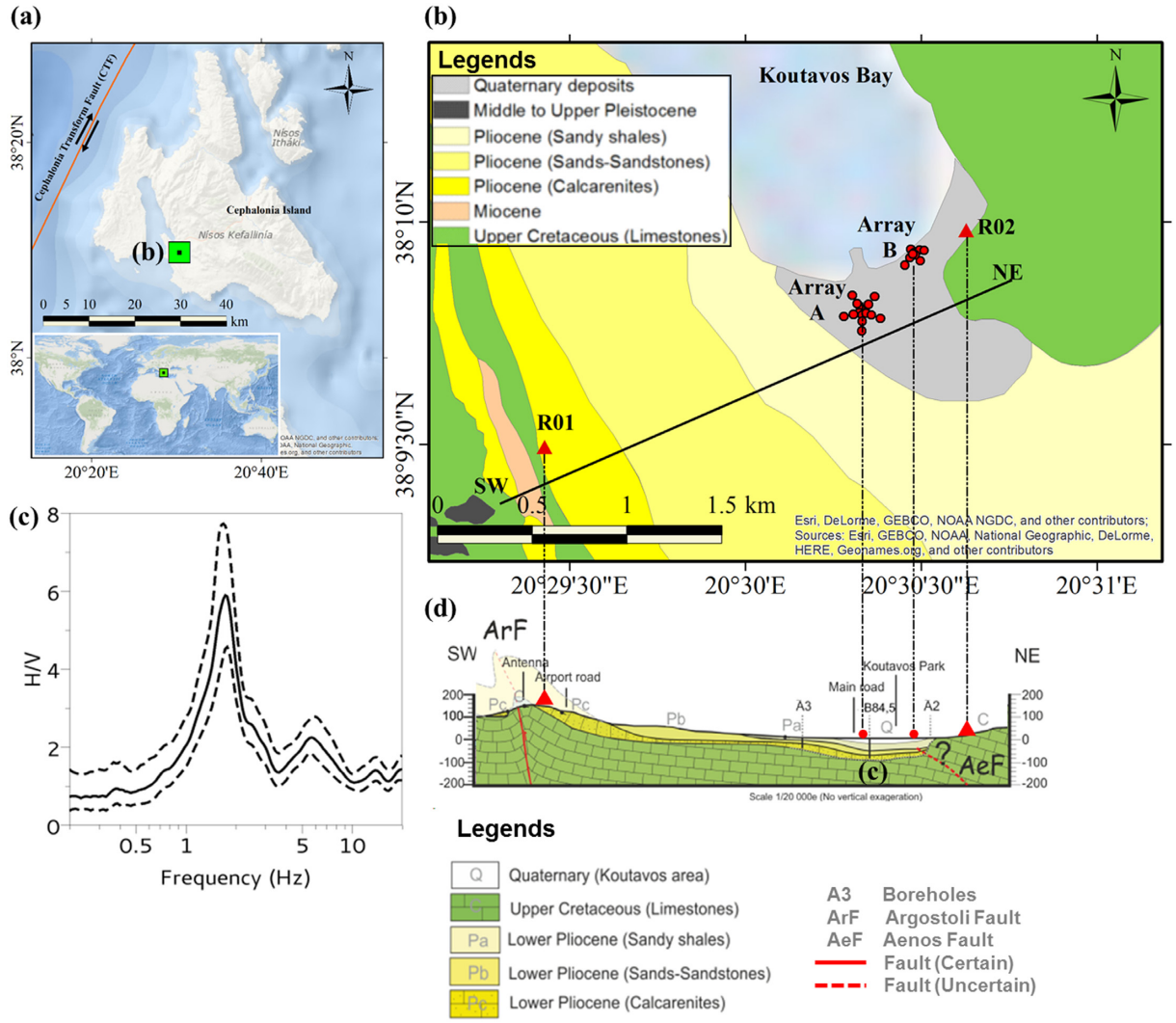

Figure 1. (a) The Argostoli study area, marked by the green rectangle, on the island of Cephalonia. (b) Zoomed view on the geological map of Argostoli (Cushing *et al.* 2016, 2020) along with the locations of Array A, Array B and the nearby rock stations (R01, R02). (c) H/V average spectral ratios ($\pm 1\sigma$) at the centre of the valley from 1 hr of ambient noise recordings.

with a particular azimuth, slowness and frequency content. The two Cartesian coordinate axes represent the horizontal components of the wave vector k_x and k_y. The colour bar represents the power of the array response, given by

$$A\left(\vec{k}\right) = \left| \frac{1}{N} \sum_{i=1}^{N} e^{-iR\vec{k}} \right|. \tag{16}$$

The limits k_{min} and k_{max} are determined from the array response and are marked by the two black circles on the plots. The diameter of the central lobe designates the array resolution limit k_{min} and of the larger circle encompassing the side lobes marks spatial aliasing limit k_{max}. In theory, two waves separated by the minimum wavenumber k_{min} can be resolved by the classical FK technique. k_{max} is the maximum resolvable wavenumber defined as the smallest value of k above the central lobe with $A(k) > 0.5$ (Wathelet *et al.* 2008). The width of the array response can be determined by k_{max}/k_{min}. From Fig. 2(c), it seems that the regular geometry of the Array A result in a good resolution capacity in all directions. However, because of its irregular configuration, the resolution of Array B seems relatively narrower (Fig. 2d). Figs 2(e) and (f) show the slowness curves, as a function of frequency, corresponding to the constant wave number values $k_{min}/2$ (continuous line), k_{min} (first dash-dotted line), $k_{max}/2$ (second dotted-dashed line) and k_{max} (dashed line). The theoretical minimum wavenumber k_{min} is 0.0558 rad m^{-1} for Array A and 0.1152 rad m^{-1} for Array B and the maximum wavenumber k_{max} is 1.13127 rad m^{-1} for Array A and 0.6838 rad m^{-1} for Array B. The width of the resolution (k_{max}/k_{min}) of Array A is about 4 times larger than that of Array B.

The V_s profiles at the two array locations, obtained from the inversion of the dispersion curves retrieved from active and passive geophysical surveys (Boxberger *et al.* 2014), are presented in Figs 3(a) and (b). They represent the velocity profiles that explain the observations (i.e., the measured dispersion curves) equally well within their uncertainty bounds. It is to be noted that they are not the best misfit profiles; hence there is no one 'best' velocity profile. The ranges of V_s profiles associated to these inverted ground models are presented in Table 1. The V_{s30} was estimated to be around 250 m s^{-1} for both locations. Since there is no estimation of intrinsic Q_P and Q_S in Argostoli, we used $Q_P = 50$ and $Q_S = 25$ in the sediments. Density is also unknown and we fix it to 2000 kg m^{-3} in the sediments and 2500 kg m^{-3} in the bedrock. The theoretical

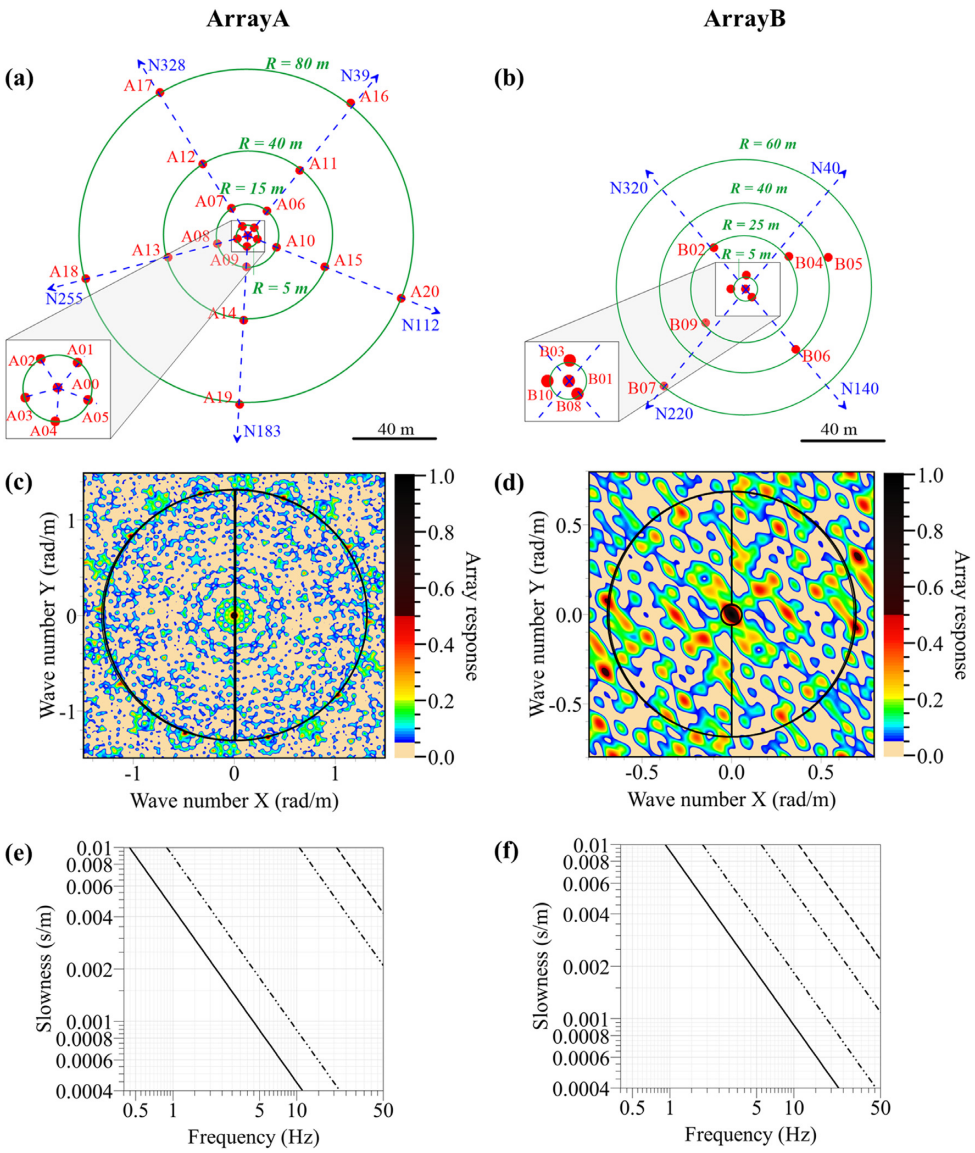

Figure 2. (a and b) Array layouts, (c and d) theoretical array response functions for the adopted layouts and (e and f) resolution limits of ArrayA and ArrayB, respectively. The four exponential lines in (e) and (f) represent the constant wave number values $k_{min}/2$ (continuous line), k_{min} (first dotted-dashed line), $k_{max}/2$ (second dotted-dashed line), k_{max} (dashed line).

dispersion curves, in terms of phase slowness, obtained from the ensembles of these V_s profiles are illustrated in Figs 3(c) and (d). The dispersion curves are calculated for the first four modes. Each mode has its own resonance frequency and shows characteristic phase behaviour. Similarly, the first four modes of Rayleigh wave ellipticity estimates from the aforementioned velocity models are presented by grey curves in Figs 3(e) and (f). The respective average estimates are shown by red-to-orange curves. For both arrays, for the fundamental mode, the ellipticity curve exhibits a singular peak and a trough, and becomes flat at higher frequencies. The Rayleigh wave motion is prograde between the peak and trough frequencies (i.e., the right flank of the peak) while it is retrograde at other frequencies. We can see multiple peaks and troughs for the higher modes. At higher frequencies (> 2.6 Hz), we observe more complex mixing of motion types and harmonic modes.

A comparison of 1-D site response terms (i.e., the transfer function) calculated for vertically incident and horizontally polarized shear (*SH*) waves, from the ensemble of the velocity models, with respect to a reference homogeneous half-space is presented by light grey curves in Figs 3(e) and (f). The average of these 1-D transfer functions (TF) is shown by the yellow curve. The average H/V ratios calculated from 1 hr of ambient noise recorded at the two array sites are presented by the black curves. The ambient noise is generally a mix of body and surface waves. Therefore, the H/V ratio corresponds to the definition of the ellipticity curve when the wavefield consists only of Rayleigh waves and to a mixture of Rayleigh, Love and *S* waves otherwise (Bonnefoy-Claudet *et al.* 2008; Lunedei & Albarello 2010). More recently, H/V ratio has been interpreted by assuming the ambient noise wavefield to be diffuse and equipartitioned (e.g. Sánchez-Sesma *et al.* 2011; Kawase *et al.* 2015; Lontsi *et al.* 2015). For Array A, the resonance frequency is at 1.52 Hz from the fundamental ellipticity curve, while it is at 1.62 Hz from H/V and 1-D site transfer function for vertically incident *S* waves. H/V computed at the centre of Array A (A00) with the underlying assumption of diffuse wavefield also provides a resonance frequency around 1.6 Hz (Tchawe *et al.* 2020). For Array B, the H/V peak is at

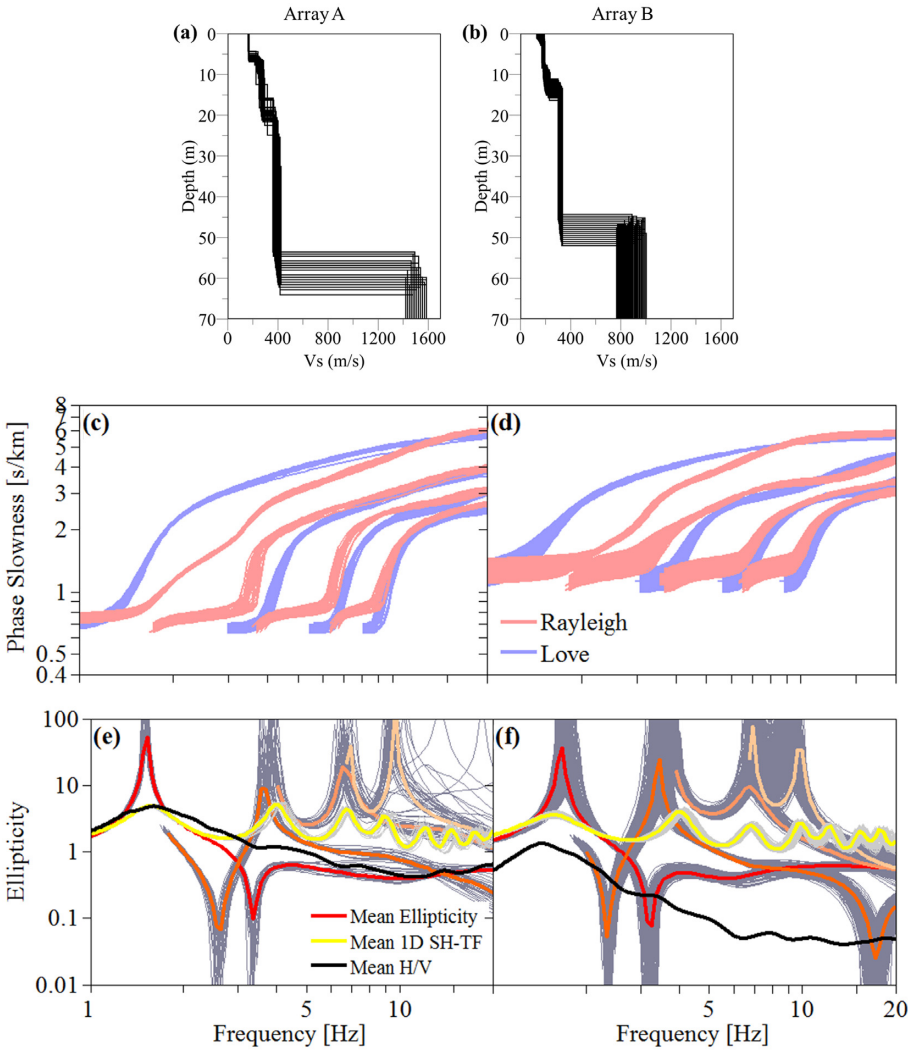

Figure 3. (a and b) Shear-wave velocity profiles inverted from the dispersion curves obtained from geophysical surveys (Boxberger *et al.* 2014) for Array A and Array B, respectively. (c and d) First four modes of theoretical dispersion curves for Love and Rayleigh waves for these velocity profiles. (e and f) Theoretical ellipticity curves (in dark grey) and their respective averages (in red to light orange), obtained from the V_s models. Theoretical 1-D transfer functions (in light grey) obtained from the V_s models, and their average (in yellow). The average H/V ratio calculated from ambient noise recorded at the centres of the arrays (in black).

1.5 Hz, while the fundamental ellipticity and 1-D transfer function peaks are at 1.67 Hz.

3.3 Data set of seismic events

The size of the Argostoli valley makes it particularly suitable for the analysis of signals from local and regional seismic events. A set of 46 events with epicentral distances (R_{epi}) of less than 200 km from station A00, with local magnitude (M_L) between 2 and 5, containing very good signal-to-noise ratio (SNR $>$ 0.5) and recorded by more than 15 stations of the array, are selected for the wavefield analysis. Most of the events are shallow, and chosen in such a way that a homogeneous distribution of magnitude, distance and azimuthal coverage can be achieved. Events at $R_{epi} \leq 80$ km have been re-localized by the Aristotle University of Thessaloniki (AUTH) seismological centre using the local network and the local crustal velocity model (FDSN 4C 2011; Imtiaz 2015; Theodulidis *et al.* 2018). For the other, mainly regional earthquakes occurring at $R_{epi} > 80$ km, the best location solutions have been taken either from the Hellenic Unified Seismographic Network (HUSN) or the European-Mediterranean Seismological Centre (EMSC). However, only 16 out of these 46 events have been recorded by Array B. The characteristics of these events are provided in Table 2 and their geographical locations are presented in Fig. 4.

4 ARRAY ANALYSIS WITH MUSIQUE

For each event under consideration, the three-component signals of all stations of the array are treated together. A schematic illustration of the process is provided in Fig. 5. Keeping the array resolution limits in mind, the wavefield analysis is carried out for 200 logarithmic frequency steps from 1 to 20 Hz. Based on the target frequency, signals are band-passed using a Chebyshev filter with a bandwidth of 10 per cent and are divided into smaller time windows. In this study, the length of the various considered time windows is tuned at each frequency to span over 5 full cycles. Hence, they get shorter with an increase in frequency. For instance, at $f = 1$ Hz, the length of analysed time windows is 5 s,

Table 1. Ranges of shear wave velocities (V_s) associated to the inverted ground models presented in Fig. 3(a) and (b) for Array A and Array B.

	Vs (m s^{-1})			
	Array A		Array B	
Depth (m)	Min.	Max.	Min.	Max.
0	161.8	171.7	129.5	190.9
5	165.0	242.4	169.4	194.8
10	226.1	290.0	181.7	237.1
15	249.8	317.2	206.2	335.8
20	267.8	386.0	301.0	335.8
25	360.1	409.8	301.0	335.8
30	360.1	418.0	301.0	335.8
35	360.1	426.4	301.0	335.8
40	360.1	426.4	301.0	335.8
45	360.1	426.4	301.0	926.6
50	360.1	426.4	319.5	1003.4
55	374.7	1524.0	767.0	1003.4
60	397.7	1585.8	767.0	1003.4
65	1421.4	1585.8	767.0	1003.4
70	1421.4	1585.8	767.0	1003.4

while at $f = 20$ Hz, it is 0.25 s. We allowed 50 per cent overlapping between two consecutive windows. For each time window, the MUSIQUE algorithm is applied in order to retrieve the back-azimuth (θ) and slowness (s) of the dominant waves crossing the array. The Chebyshev filter just removes the outlier frequencies. The results are not sensitive to its bandwidth. The windows are overlapped only for smoothing the results. However, it is important to include at least 5 cycles of signal in the analysis windows in order to ensure that the time windows are short enough to capture the specific target seismic phases. It also provides more robust and stable solutions.

For each time window, the total energy is calculated as the sum of the energies of all three components and all stations of the array. In this work, we have considered a stringent energy-based criterion to distinguish between Love and Rayleigh waves. If the transverse energy in an analysed window is larger than 70 per cent of the total energy, the dominant wave is characterized as a Love wave. The sum of the transverse energies of all stations of the array corresponding to the attributed windows is taken as the Love wave energy. On the other hand, if the combined radial and vertical energy in a window is larger than 70 per cent of the total energy, the dominant wave is characterized as a possible Rayleigh wave. The sum of the radial and vertical energies of all stations of the array corresponding to the Rayleigh waves is taken as the Rayleigh wave energy. No wave is identified if none of these criteria is fulfilled, in other words, the window remains "uncharacterized". The retrograde or prograde particle motion is identified from the estimated phase difference (φ) values. In theory, $\varphi = 90^\circ$ corresponds to retrograde and $\varphi = 270^\circ$ corresponds to prograde particle motion. In this work, φ values ranging from 45° to 135° are identified as retrograde and from 225° to 315° as prograde in order to account for possible estimation errors. For other values of φ, the window remains "uncharacterized". It is worth mentioning here that the original MUSIQUE algorithm uses a 50 per cent energy threshold for the identification of the two types of surface waves (Hobiger 2011). However, we observed that this threshold was not discriminant enough in our case and it leads to the inclusion of some wave energies that could not be characterized as Love or Rayleigh with confidence. We found out that a 70 per cent energy threshold was more efficient for our data.

The preliminary results obtained from the MUSIQUE analysis are post-processed in order to present them in a meaningful way. Lagged coherency, a measure of similarity between two seismic motions at a particular frequency, is calculated for all the available station pairs. Its values range from 0 for uncorrelated to 1 for perfectly correlated signals. Details of the coherency calculation are provided in (Imtiaz *et al.* 2018a,b). For each time window, the mean coherency (COH_m) is determined by averaging the individual coherency from all station pairs. For each earthquake, results obtained from time windows containing $COH_m < 0.5$ are excluded in order to avoid incoherent signal blocks. Keeping the spatial aliasing limits of the arrays in mind, only windows corresponding to $0.0004 \leq s \leq 0.008$ s m^{-1} (i.e., phase velocities between 125 and 2500 m s^{-1}) for Array A and to $0.0004 \leq s \leq 0.0035$ s m^{-1} (i.e., phase velocities between 285 and 2500 m s^{-1}) for Array B are included in the analysis. In order to homogenize the contributions from all windows, their energies are normalized by the respective mean squared Fourier Amplitude Spectra (FAS_m), obtained by averaging the estimates from all three components of all stations.

5 RESULTS

The post-processed results from the MUSIQUE analysis are summarized in the following segments.

5.1 Results from a single seismic event

First, we present the results obtained from the array analysis of a single event (Event ID 12 in Table 2). It occurred on 14th October 2011 at 01:11:32 UTC with a local magnitude of $M_L = 3.5$, at a hypocentral depth of 12 km, epicentral distance of 36 km, and a backazimuth of N 125å from the central station A00. Fig. 6(a) shows the location of the event with respect to the site. Fig. 6(b) to Fig. 6(d) display the waveforms recorded at the hard rock station (R02), at the central station (A00) of ArrayA, and at the central station (B01) of ArrayB, respectively. When compared to the signals from station R02, amplification and duration lengthening of the seismic signals as well as locally generated surface wave trains are evident on the seismograms of the array stations A00 and B01. The wave parameters retrieved by the MUSIQUE analysis of the Array A and Array B data are discussed in the following sections.

5.1.1 Resolved wavefield parameters: backazimuth and slowness

Figs 7(a) and (b) show the backazimuth-time, and Figs 7(c) and (d) show the slowness-time distribution of the dominant waves crossing Array A and Array B. Each point on the plots represents an analysed time window. Different slowness or backazimuth values may correspond to a given time, depending on the considered frequency band. The colour bar indicates their normalized energy. We can clearly distinguish the onsets of *P*- and *S*-wave arrivals as well as the approximate duration of the main phase of the signal through the changes of the energy content. Energetic waves seem to be coming from a wide range of different backazimuths (N 60°–N 240°) rather than the direction of the earthquake epicentre (marked by the red line), indicating strong diffraction of the waves. We can also see that these waves are propagating at a wide range of slowness (0.0004–0.004 s m^{-1}, i.e., 250–2500 m s^{-1}) at any given time, depending on the considered frequency band.

Table 2. Catalogue of the analysed earthquakes. See Fig. 4 for a map of the epicentres. ID is the index. The date and time (in UTC) of occurrence are given as YYYYMMDD_hhmmss. M_L is the local magnitude and H is the hypocentral depth of the earthquake. R_{epi} is the epicentral distance and Baz is the backazimuth of the earthquake with respect to station A00.

ID	Origin date/time	M_L	H (km)	R_{epi} (km)	Baz (N°)	Array Data
1	20110922_151509	3.3	17.60	10.20	259.81	A
2	20110924_030834	2.7	7.00	74.50	285.43	A, B
3	20110924_154912	3.1	14.40	101.90	221.93	A, B
4	20110928_074045	3.5	16.90	13.50	221.33	A, B
5	20110930_003052	2.0	4.60	17.80	314.70	A, B
6	20111008_032445	2.8	6.10	51.10	7.48	A, B
7	20111008_205900	2.8	14.80	69.10	286.62	A, B
8	20111009_184220	3.3	17.00	91.70	117.36	A, B
9	20111010_025743	2.8	13.70	18.90	333.76	A, B
10	20111010_190700	4.5	11.00	173.20	128.12	A, B
11	20111012_045443	2.3	2.20	15.30	237.52	A, B
12	20111014_011132	3.5	11.90	36.10	125.50	A, B
13	20111016_100137	2.7	17.60	13.40	283.33	A, B
14	20111017_100004	3.1	37.00	81.30	7.02	A
15	20111020_061820	3.4	16.50	8.80	134.00	A
16	20111020_073537	2.8	9.20	15.20	205.56	A
17	20111020_204020	2.2	16.50	9.70	142.43	A
18	20111025_223304	4.1	13.90	34.60	119.35	A
19	20111031_072250	2.6	0.10	6.20	2.80	A
20	20111031_204035	2.8	13.10	14.70	220.28	A
21	20111110_172539	4.6	19.00	119.30	75.78	A, B
22	20111110_231028	2.7	2.90	65.00	359.50	A
23	20111112_045148	2.5	0.50	77.50	181.15	A
24	20111115_141004	3.7	16.80	60.70	149.20	A, B
25	20111124_040923	3.6	36.00	149.10	336.45	A
26	20111128_032308	3.2	16.50	7.90	172.67	A
27	20111208_090935	2.9	9.70	38.90	194.91	A
28	20111215_000742	3.1	14.00	92.70	218.71	A, B
29	20111215_170549	2.7	20.00	131.50	182.93	A, B
30	20120119_234608	2.2	10.00	46.20	354.64	A
31	20120214_132143	4.3	13.00	56.40	155.59	A
32	20120303_230430	1.9	12.60	40.10	356.44	A
33	20120314_214443	2.9	0.00	56.30	215.98	A
34	20120315_054058	4.4	15.00	90.70	49.63	A
35	20120317_023659	2.4	31.20	44.30	123.58	A
36	20120320_185051	3.0	18.50	3.10	74.21	A
37	20120321_055047	3.8	16.00	116.30	64.40	A
38	20120327_143302	2.0	18.80	13.10	94.50	A
39	20120404_014530	3.4	19.00	94.80	95.94	A
40	20120410_134545	2.5	12.40	26.10	250.92	A
41	20120410_215535	2.2	11.80	39.90	5.83	A
42	20120411_061851	3.7	9.00	167.50	356.90	A
43	20120415_132543	2.4	16.00	16.30	293.97	A
44	20120415_221904	2.1	13.10	29.50	18.17	A
45	20120416_084022	3.6	17.00	143.90	83.44	A
46	20120416_112342	5.2	33.00	190.30	150.92	A

For a better view of the results, we present the backazimuth-time distribution in Figs 8(a) and (b), where the corresponding axes are divided into grids of 5° by 1 s. The colour bar indicates the sum of normalized energy of the windows falling into each grid. For both arrays, we can clearly identify the most energetic phase lying between 6.5 and 15 s (marked by the black vertical lines). It corresponds very well with the signals from the NS component of the central stations of the arrays shown in Figs 8(c) and (d). During this phase, the waves are coming mainly from N 210° ± 30° to Array A and from N 90° ± 30° to Array B.

The backazimuth-frequency distribution of the dominant waves from the Array A and Array B data are presented in Figs 9(a) and (b), respectively. The frequency axis has a grid step of 0.02 on a logarithmic scale and the backazimuth axis has a grid step of 5°. The colour bar indicates the sum of normalized energy of the windows falling into each grid. We can see that most of the wave energy of Array A arrives around N 210° between 1 and 3 Hz. At higher frequencies, the waves are more scattered, but still arriving from around N 210°. For Array B, however, the waves seem to be arriving from the directions between N 90° and N 120°.

The slowness–frequency distribution of the dominant waves from the Array A and Array B data are presented in Figs 9(c) and (d), respectively. We observe that the phase velocities are mostly frequency-dependent, indicating the presence of dispersive surface waves. For Array A, we can observe a possible fundamental-mode dispersion trend between 1 and 3 Hz, and probable higher modes at higher frequencies. The mode trends, however, are less clear for Array B.

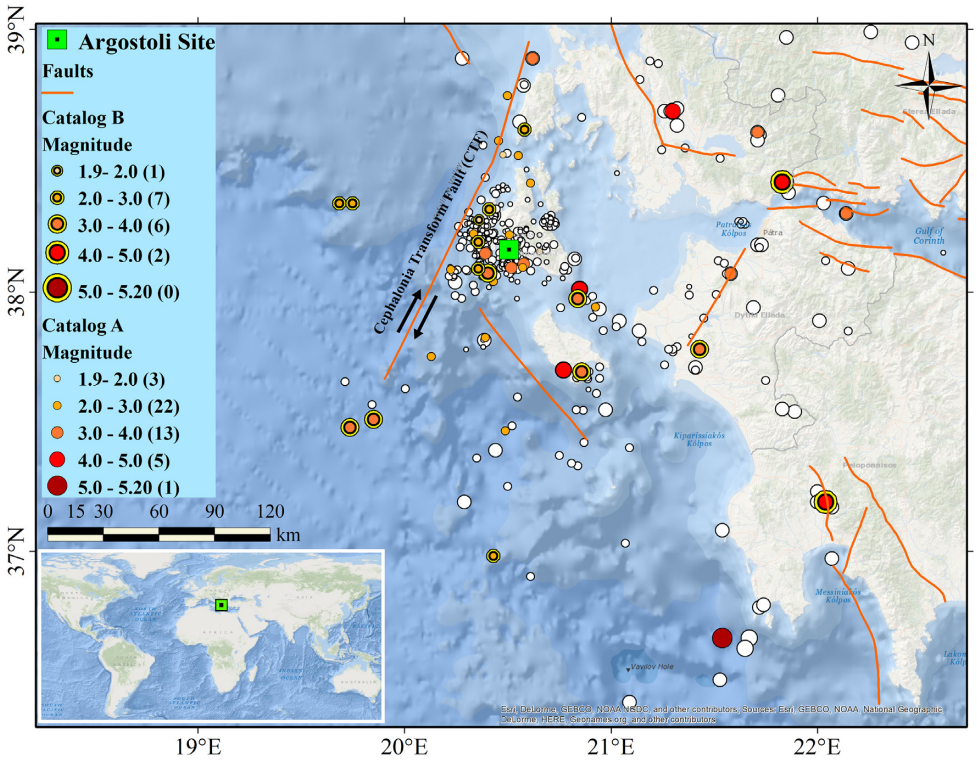

Figure 4. Location of the selected events (Table 2) recorded by two dense arrays (Array A and Array B). White circles show other events recorded during the seismological experiment.

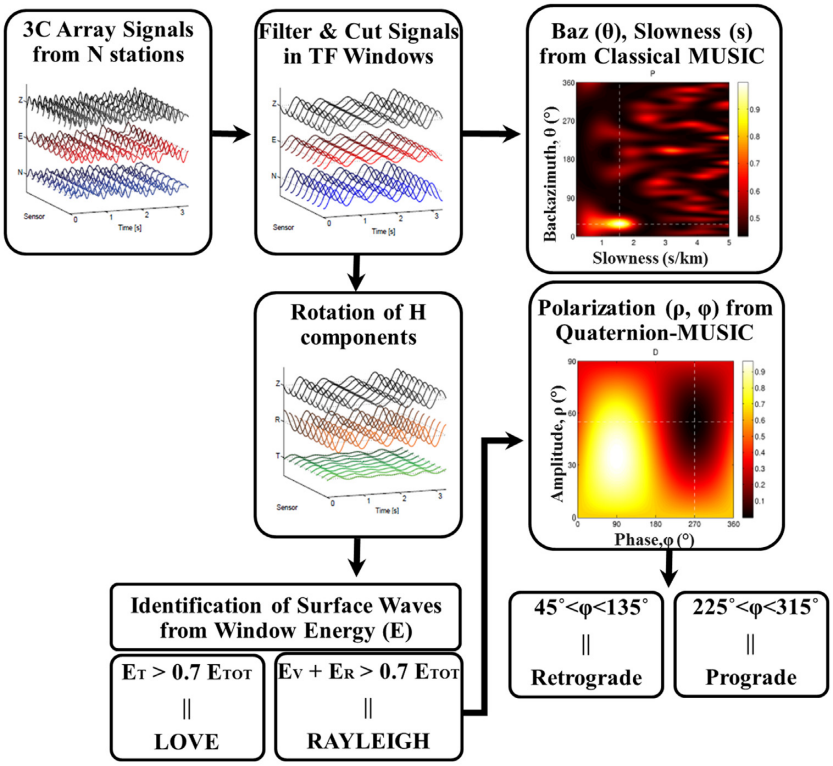

Figure 5. Schematic representation of the different steps of the MUSIQUE algorithm (Modified from Hobiger 2011).

5.1.2 Energy repartition between Love and Rayleigh waves

Fig. 10 shows the distribution of Love and Rayleigh wave energies within a given frequency range for 10° backazimuth intervals. The energy is presented on a logarithmic scale for a better visualization of the lower values. The subplots correspond to three frequency ranges (1–1.5, 1.5–2 and 2–2.5 Hz) around the fundamental resonance frequency of the valley (f_0~1.5 Hz) and all frequencies

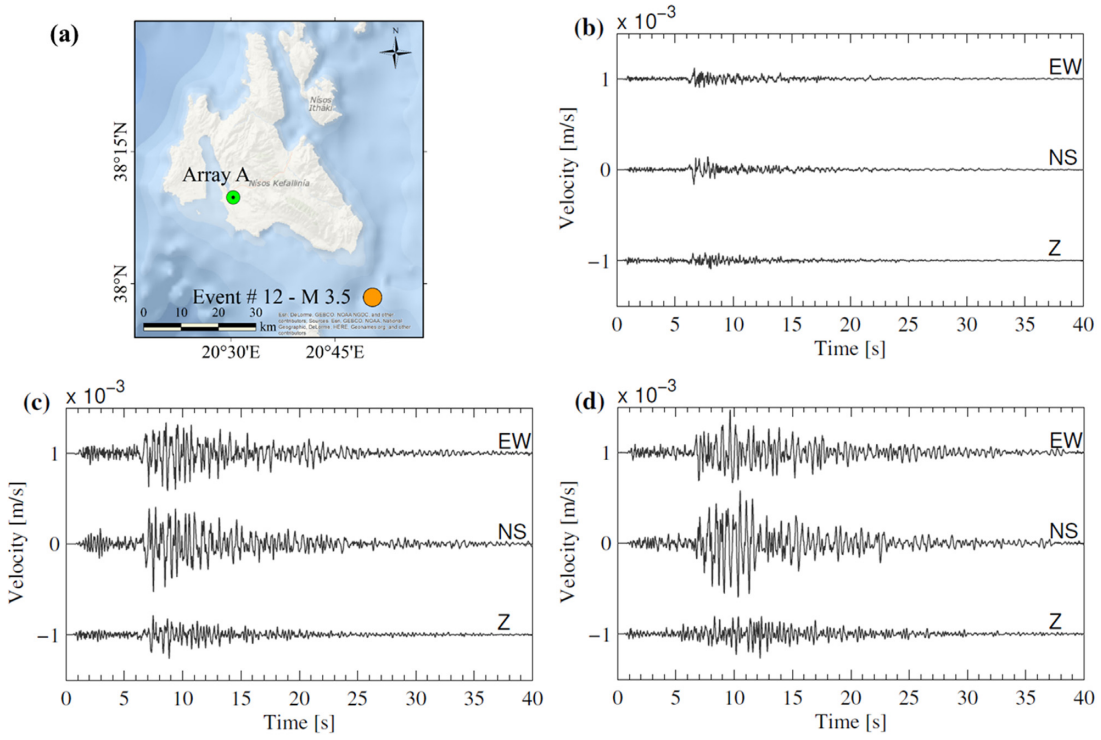

Figure 6. (a) Geographic location of event no. 12 (Origin Date = 2011/10/14, Origin Time = 01:11:32 UTC, $M_L = 3.5$, Baz = N 125°, $R_{epi} = 36$ km, $H = 11.9$ km). 3C Velocity time series of the event recorded (b) at the rock station R02, (c) at the central station A00 of Array A, and (d) the central station B01 of Array B.

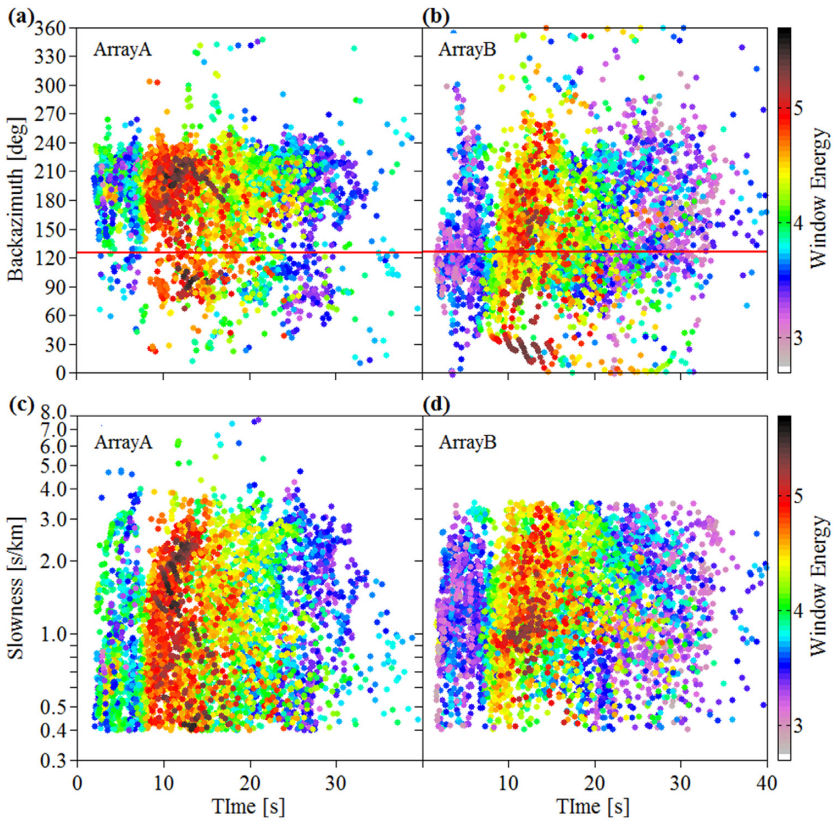

Figure 7. (a and b) Backazimuth-time and (c and d) slowness-time distribution of the dominant waves obtained from the MUSIQUE analysis. The colour bar indicates the estimated energy of each analysed window represented by the points on the plot. The red horizontal line in (a) and (b) indicates the direct backazimuth of the event.

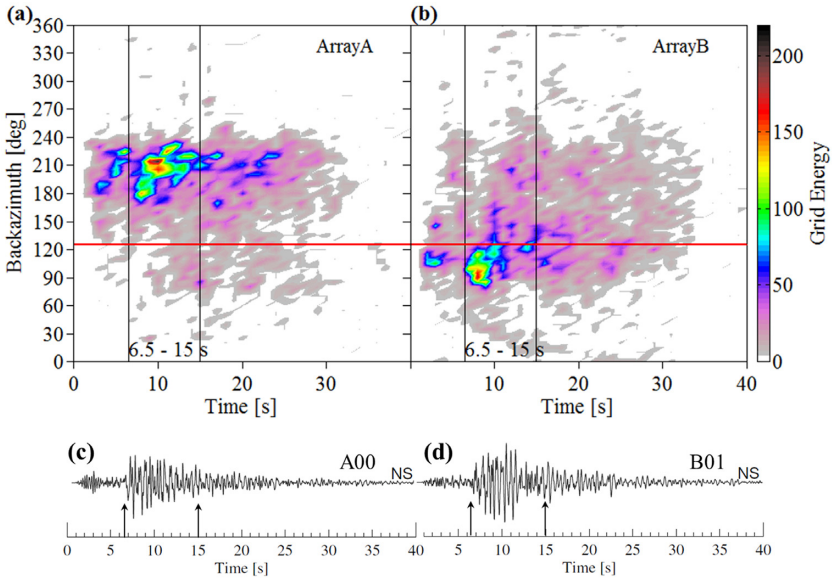

Figure 8. (a and b) Grid representation of the backazimuth-time distribution obtained from the MUSIQUE analysis of event no. 12. The colour bar indicates the total energy represented by the grid points. The black vertical lines mark the approximate times of the most energetic phase from 6.5 to 15 s. (c and d) NS component of the velocity time series recorded by the two central stations A00 and B01. The black arrows mark the aforementioned time window.

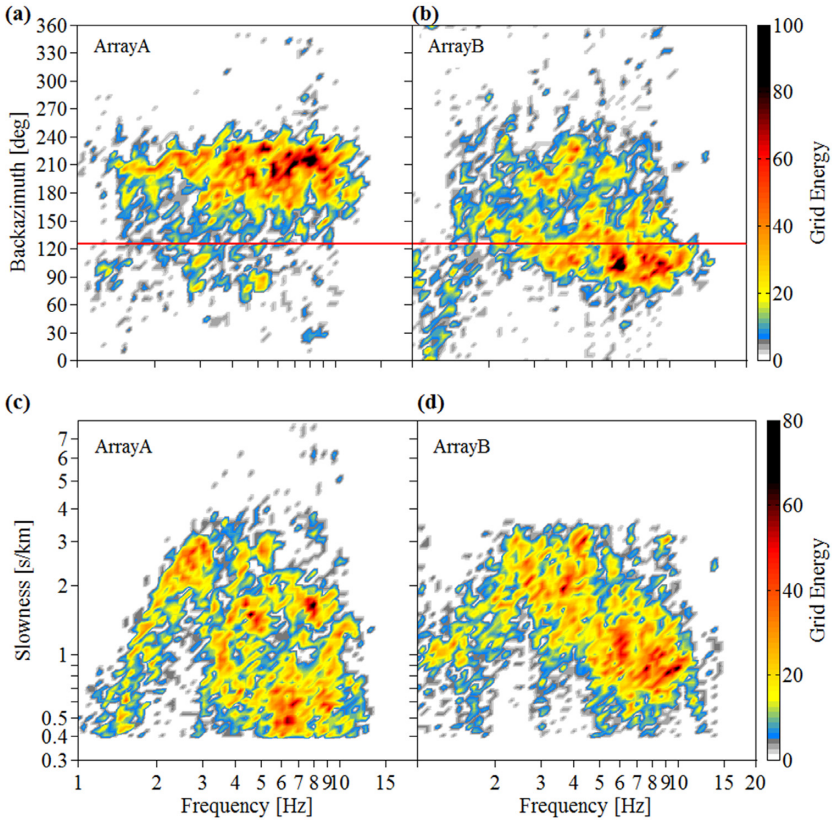

Figure 9. (a and b) Grid representation of the backazimuth-frequency distribution and (c and d) slowness-frequency distribution from the MUSIQUE analysis of event no. 12. The colour bar indicates the normalized energy represented by the grid points. The red horizontal lines in (a) and (b) indicate the direct backazimuth of the event.

combined (1–20 Hz). On each subplot, red and green lines represent the Rayleigh and Love waves, respectively, and the blue dot marks the backazimuth of the event. In case of Array A (Figs 10a–d), the dominance of Love waves is evident at all frequencies. We observe that the surface wave energies are scattered mainly between N 60° and N 240° directions, which could be associated with two edges of the valley. A rather significant proportion of energy, dominated by Love waves, seems to be arriving from the southwest (N 180°–N 240°). When all frequencies are combined, the scattering seems to occur in a broader azimuthal range between these two principal

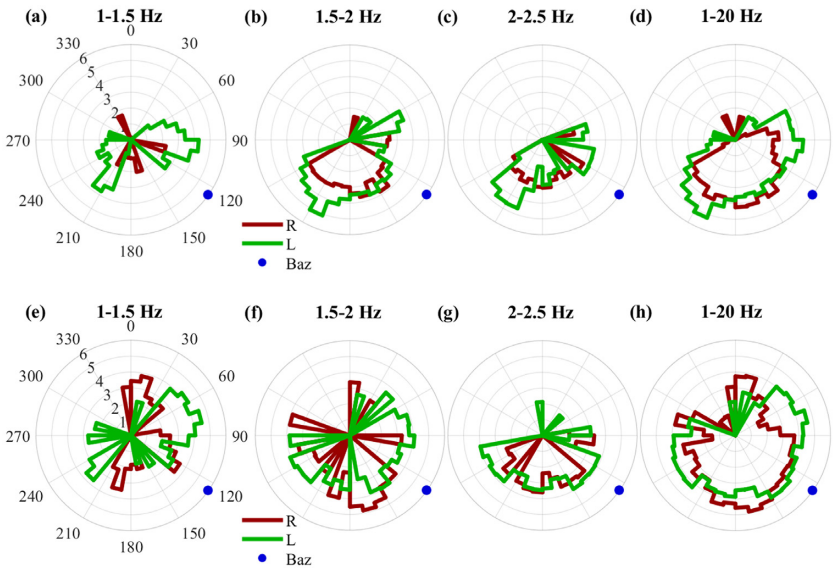

Figure 10. Polar distribution of the Love (L) and Rayleigh (R) wave energies for the different 10 degree intervals in different frequency ranges for (a)–(d) Array A and (e)–(h) Array B data from event no. 12. The blue dot indicates the backazimuth (Baz) of the event.

directions. In case of Array B (Figs 10e–h), we observe a relatively higher contribution from the eastern direction and Rayleigh waves.

Figs 11(a) and (b) present the energy repartition between Love and Rayleigh waves as a function of frequency for the same event and for both arrays. The respective energies are estimated as a percentage of the total window energy. Overall, the contribution of identified surface waves decreases with increasing frequency. In case of Array A (Fig. 11a), more than 40 per cent of the window energy between 1 and 3.5 Hz could be associated with Love waves. At higher frequencies, the wavefield becomes a mixture of both Love and Rayleigh waves, with Rayleigh waves dominating between 3 and 4 Hz. However, in case of Array B (Fig. 11b), even though Love waves dominate the wavefield up to about 3.5 Hz, we can also observe contributions from Rayleigh waves over all frequencies.

5.2 Robustness of the dominant direction of waves

In order to investigate the robustness of the observed dominant direction of waves, five events with different backazimuths and similar epicentral distances (from X to y km) are selected and the results of the MUSIQUE analysis are compared. The characteristics of these events are provided in Table 2 (Event IDs 6, 21, 24, 3 and 7) and their locations are shown in Fig. 12. The backazimuth-frequency distribution corresponding to these events for Array A and Array B are also presented in the same figure. For both arrays, no matter what the event backazimuth is, we observe a consistent trend in terms of the principal direction of diffraction. The most dominant direction lies between N 210° and N 240° for Array A, while it is between N 60° and N 120° for array B. These two directions are close to the southwestern and northeastern edges of the valley, respectively. Interestingly, the estimates from Array A do not show a strong diffraction from the northeast, but those from Array B indicate a second dominant diffraction from the southwest direction. This observation is more evident when the event backazimuth lies between the two directions (e.g. Event no. 21 and 24). This indicates that the diffraction generated by the southwest edge is strong enough to be also observed by the Array B.

5.3 Analysis of diffracted wavefield

This section summarizes our main observations by combining results of all events from each array. In order to focus only on the diffracted wavefield, we eliminate the contributions from direct arrivals (i.e. from the direction of the earthquake) by excluding the results corresponding to each event's backazimuth ± 20°. The remaining results are stacked together and presented in backazimuth-frequency and slowness-frequency planes over rectangular grids. The colour bar represents the sum of normalized energy from all the event windows falling between the grids. It is to be noted that in this paper, the terminology 'diffracted waves' is adopted to refer to the laterally propagating surface waves diffracted at the edge of the basin.

5.3.1 Backazimuth

The summary of the backazimuth-frequency distribution of the diffracted wavefield is shown in Figs 13(a)–(c) for Array A and in Figs 13(d)–(f) for Array B. The subplots from left to right present the results associated with the entire diffracted wavefield (All = Love + Rayleigh + Uncharacterized), Love waves, and Rayleigh waves, respectively. In case of Array A (Fig. 13a), we observe dominant scattering of the waves over the entire frequency range from the southwest direction (N 210° ± 30°), as noted earlier. However, some scattering is also observed at lower frequencies (< 3 Hz) between N 60° and N 180° directions. Diffracted Love waves dominate frequencies below 3 Hz (Fig. 13b), while both Love and Rayleigh waves contribute at higher frequencies (Fig. 13 (c)). In case of Array B (Fig. 13d), the most dominant diffraction is seen from the east (N 90° ± 30°) direction over all frequencies. Relatively high energies are also observed between N 120° and N 240° at frequencies below 4 Hz. Some diffraction from directions between N 0° and 60° is also observed below the fundamental resonance frequency (1.5 Hz) of the site. Figs 13(e) and

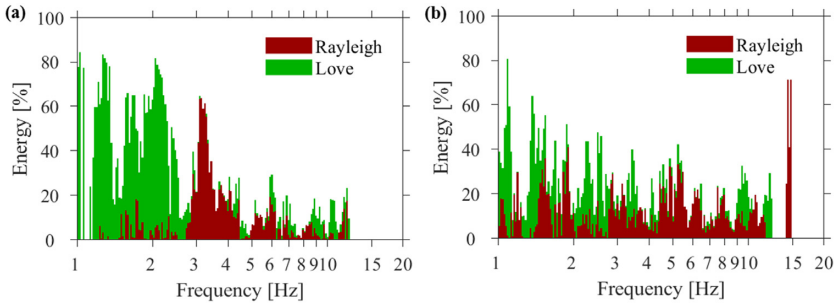

Figure 11. Proportion of Love and Rayleigh wave energy with respect to the total window energy, as a function of frequency, for (a) Array A and (b) Array B data for event no. 12.

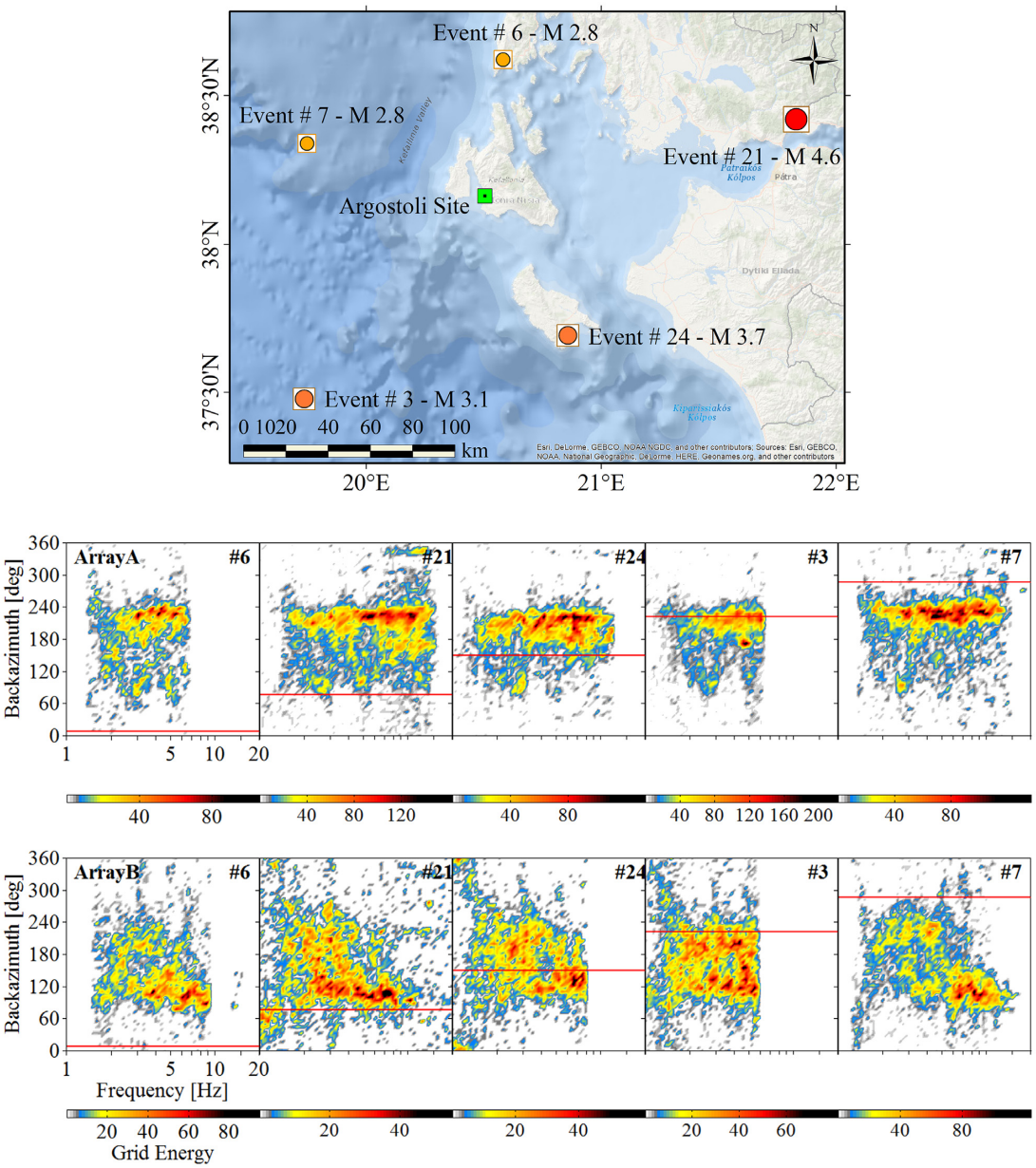

Figure 12. Top: location of the epicentres of five earthquakes (Events no. 6, 21, 24, 3 and 7) occurring at different backazimuths around the site. Bottom: grid representation of the backazimuth-frequency distribution of the corresponding events from Array A and Array B data (bottom).

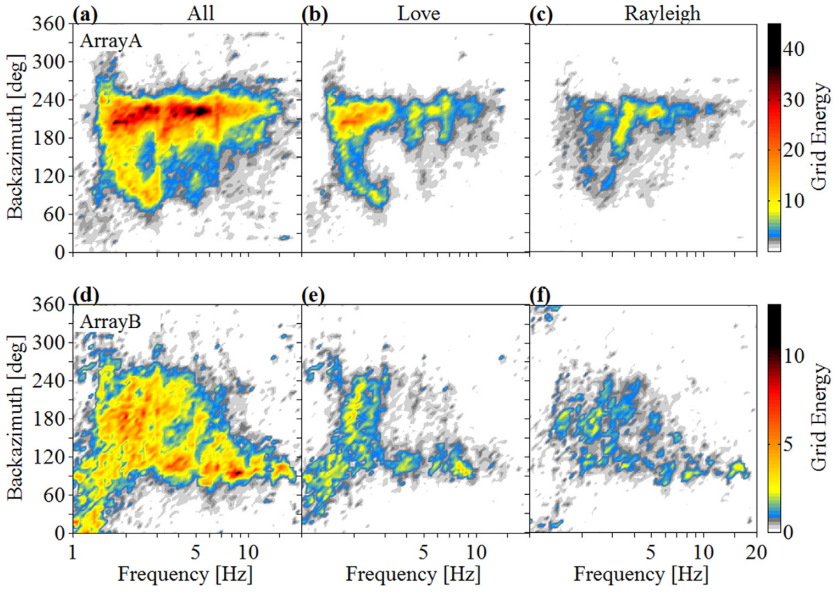

Figure 13. Grid representation of the summary of the backazimuth-frequency distributions for diffracted waves obtained from the MUSIQUE analysis of all events for (a)–(c) Array A and (d)–(f) Array B data. The plots from left to right correspond to all diffracted waves, diffracted Love waves, and diffracted Rayleigh waves, respectively. The colour bar indicates the summed normalized energy represented by the grids.

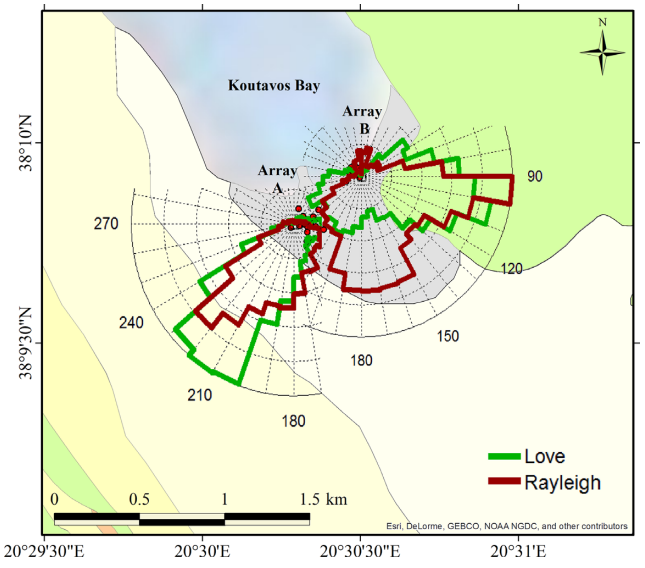

Figure 14. Direction of dominant diffracted surface wave arrivals for Array A and Array B. The two radial diagrams represent the respective distribution of the identified Love and Rayleigh wave energies for 10-degree intervals and all frequencies between 1 and 20 Hz.

(f) show that Love waves mostly dominate the lower frequencies (<3 Hz) and a mix of Love and Rayleigh waves contribute at higher frequencies.

For a simpler visualization of our observations, we present the radial distributions of Love and Rayleigh wave energies in Fig. 14, by considering all frequencies (1–20 Hz) together at 10° backazimuth intervals. The summary obtained from each array is superimposed on the respective locations at the site. It seems that the propagation of both surface waves takes place between the SW and NE directions and could be associated with the 2-D/3-D geometry of the valley.

5.3.2 *Slowness*

The summary of the slowness-frequency distribution of the diffracted wavefield is shown in Figs 15(a)–(c) for Array A and in Figs 15(d)–(f) for Array B. The subplots from left to right present the results associated with the diffracted Love, prograde Rayleigh, and retrograde Rayleigh waves, respectively. The black curves represent the average of theoretical phase velocities obtained from the ensemble of dispersion curves presented in Figs 3(c) and (d). The four curves, from left to right, correspond to the fundamental and first three higher modes of Love and Rayleigh waves. Considering MUSIQUE as a high resolution technique, we have set the lower array resolution limit to $k_{min}/2$, which is marked by the purple line. The red-to-orange horizontal curves in Figs 15(b) and (e) display the frequency bands corresponding prograde particle motions, identified from different modes of theoretical ellipticity curves presented in Figs 3(e) and (f). Similarly, in Figs 15(c) and (f), the horizontal red to light orange curves indicate the frequency bands where retrograde motion is expected from the 1-D models.

In case of Array A, we observe a very clear dispersion curve for Love waves at frequencies below 3 Hz, corresponding to the fundamental mode. Traces of higher modes of Love waves are observed between 4 and 5 Hz and between 6 and 7 Hz. The branches are in good agreement with the dispersion curves corresponding to the models shown in Fig. 3, even though the fundamental-mode slownesses of these models are slightly higher. We see prograde Rayleigh waves mainly between 1.5 and 3 Hz and between 4 and 5 Hz. Between 1.5 and 3 Hz, the data are very scattered and no clear dispersion curve can be identified, but the frequency range coincides with the prograde part of the fundamental mode ellipticity curve (red curve in Fig. 3e) obtained from the V_s model of Array A. The branch between 4 and 5 Hz coincides with the first higher mode, which seems to have a prograde particle motion above 3.6 Hz (dark orange curve in Fig. 3e). For retrograde Rayleigh waves, a very strong patch is visible between 3 and 4 Hz, in good agreement with the retrograde particle motion of the first higher mode ellipticity curve (dark orange curve in Fig. 3 (e)). A second patch at higher

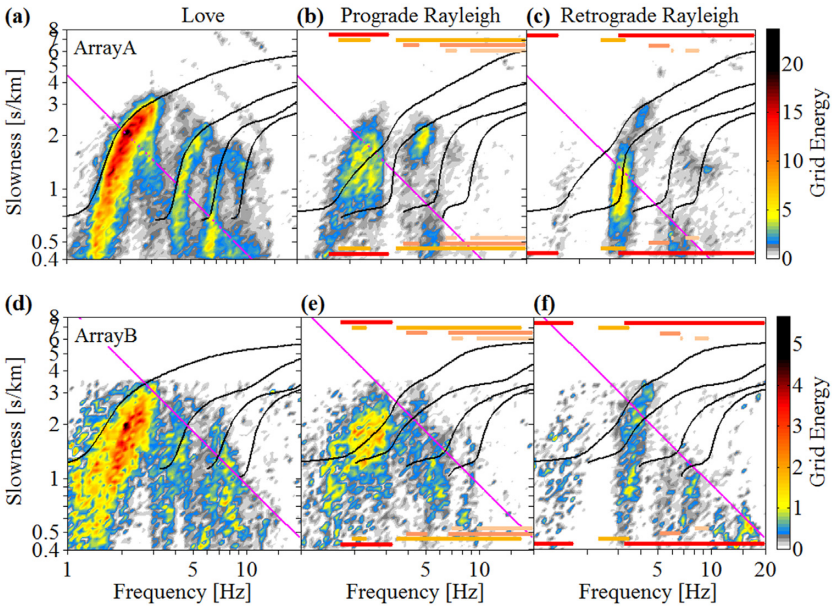

Figure 15. Grid representation of the summary of the slowness-frequency distributions, obtained from the MUSIQUE analysis of all events for (a)–(c) Array A and (d)–(f) Array B data. The plots from left to right correspond to diffracted Love waves, diffracted prograde and retrograde Rayleigh waves, respectively. The colour bar indicates the summed normalized energy represented by the grids. The purple straight line indicates the array resolution limit ($k_{min}/2$), i.e., waves with frequency and slowness to the top right are well resolved. The black curves represent the average of the theoretical dispersion curves presented in Figs 3(c) and (d). The four curves, from left to right, correspond to the fundamental and first three higher modes. The red to light orange horizontal lines in plots (b) and (e) show the bands of frequencies of prograde Rayleigh motions at different modes, as of Figs 3(e) and (f), and similarly the frequency bands of retrograde motion in plots (c) and (f).

slowness (>2 s km^{-1}) is visible between 4 and 5 Hz, which might belong to the fundamental mode.

We observe similar trends for Array B, but with more scattering. For Love waves, we can identify the fundamental mode, but the higher modes are not clear. For prograde Rayleigh waves, we can see a part of the fundamental mode between 1.7 and 3 Hz, but no clear trend for higher modes. For retrograde Rayleigh waves, a patch similar to that of Array A is visible between 4 and 5 Hz, which may belong to the first higher mode at lower slowness and the fundamental mode at higher slowness (>2 s km^{-1}). Overall, the estimated slowness values seem to be closer to the ones estimated from Array A.

The slowness estimates of MUSIQUE for the fundamental mode Love waves, seem relatively lower (higher phase velocity) than those from the theoretical approach. One explanation could be that the seismic waves measured by the active and passive geophysical measurements have limited prospecting ability compared to those arriving from the earthquakes occurring outside the valley. Hence, there might be a bias in the estimation of inverted velocity profiles due to a lack of fit at lower frequencies ($< f_0$). The theoretical estimates are also unable to capture the effects of 2-D/3-D wave propagation, if any. Moreover, at lower frequencies, the superposition of waves propagating from both edges of the valley, at about 180° difference in direction, may result in much faster speeds, which MUSIQUE might not be able to distinguish as it identifies only one 'main' wave in each time–frequency window.

It is worth noting that a part of our MUSIQUE results, especially in case of Array B, lie below the array resolution limit. Hence, we do not exclude the possibility of systematic velocity misestimation. It could be argued that the theoretical array limits only serve as a first-order proxy. Given that MUSIQUE is a high resolution technique, the empirical array resolution capacity is much wider than the theoretical one. Many studies (Lacoss *et al.* 1969; Asten & Henstridge 1984; Cornou *et al.* 2006; Gouédard *et al.* 2008; Wathelet *et al.* 2008) have also observed improved resolution capabilities when HRFK method is used. The same studies also report that for irregular 2-D array geometry, it is not very straightforward to relate the array shape with its spatial aliasing or resolution limits. It rather depends on the direction of the incident wavefield and the effective smallest/largest interstation distance along the wave propagation direction. Hence, in case of Array B, we believe that the theoretical array response does not accurately reflect the experimental resolution limit. For both arrays, we observe a satisfactory agreement between the MUSIQUE estimates and the theoretical phase slowness curves obtained from the inverted velocity models. Hence, we believe that our results are reliable enough to be further interpreted.

5.4 Wavefield composition and site amplification

Figs 16(a) and (b) illustrate the arithmetic means of diffracted Rayleigh and Love wave energy, within one standard deviation (σ), as a percentage of the 'total analysed energy' (all direct and diffracted waves, all events) for Array A and Array B, respectively. On average, about 40 to 60 per cent of the 'total analysed energy' from both arrays is characterized as diffracted Love and Rayleigh waves. Love waves are generally more prevalent than Rayleigh waves, especially at lower frequencies (1–3 Hz), while certain narrow bands of higher frequencies are dominated either by Love or Rayleigh waves.

We also investigated whether our results are consistent with the estimates obtained from the active and passive geophysical surveys, and could provide physical implications for interpreting the

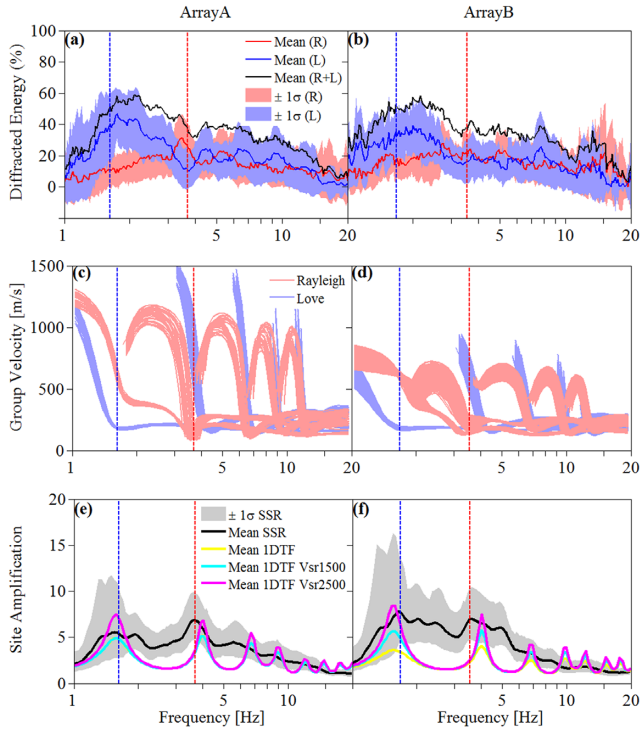

Figure 16. (a and b) Repartition of energy carried by diffracted Rayleigh (R) and Love (L) waves, estimated from the MUSIQUE analysis of all events from Array A and Array B data, respectively. (c and d) Theoretical group velocities for the first five modes of Love and Rayleigh waves obtained from the ensemble of V_s profiles presented in Figs 3(a) and (b). (e and f) Estimates of standard spectral ratio (SSR) from the horizontal components of station A00 and KES04 (next to station B04) (Cultrera *et al.* 2014; Theodoulidis *et al.* 2018); mean of 1-D *SH* transfer functions (TF) (in yellow) obtained from the V_s models presented in Figs 3(a) and (b); mean of 1-D *SH* TF for the same V_s models by assuming a constant bedrock velocity (V_{sr}) of 1500 m s^{-1} (in cyan) and 2500 m s^{-1} (in magenta).

observed site amplification. Theoretical group velocities for the fundamental and first four higher modes of Rayleigh and Love waves, obtained from the ensemble of inverted V_s profiles (Figs 3a and b), are presented in Figs 16(c) and (d). Group velocity is the velocity in which the overall envelope of the wave energy moves and is generally slower than the phase velocity. Energetic waves are often associated with local minima of the group velocity, corresponding to the Airy phase (James 1989). For Array A, the Airy phase occurs at around 1.62 Hz for the fundamental mode of Love waves, and at 3.67 Hz for the fundamental and first higher mode of Rayleigh waves. These two points on the frequency axis are marked by a blue and a red dashed line, respectively. Surface wave trains around these frequencies are supposed to be travelling at the same velocity and are arriving at once at the array, thus superimposing a large amount of energy. We can clearly identify the largest proportion of Love and Rayleigh wave energies around these Airy phases in Fig. 16(a). Similar observations can be made for Array B at around 1.67 Hz for Love waves and at 3.54 Hz for Rayleigh waves.

We estimated the site amplification in terms of the Standard Spectral Ratio (SSR) at one station from each array site. SSR is defined as the ratio of the Fourier amplitude spectrum of a soil-site record to that of a nearby rock-site record from the same earthquake and the same component of motion. Assuming source and path effects are the same for both records, SSR reflects the effect of local soil conditions at the site. We estimated this ratio for the two horizontal components at A00 (central station of Array A) and at another station (KES04) right next to the station B04 of Array B. As enough earthquakes were not recorded by the Array B, we used the KES04 station instead, which was part of the NERA experiment (see, Theodoulidis *et al.* 2018). We considered the hard rock station R02 as a reference for both sites. We used signals from 164 earthquakes recorded by these stations (Cultrera *et al.* 2014; Theodoulidis *et al.* 2018). The geometric mean of the SSRs computed at the sedimentary stations A00 and KES04 are presented in Figs 16(e) and (f), respectively. The theoretical 1-D *SH* transfer functions are shown by the yellow curves for ground models presented in Figs 3(a) and (b). They represent bedrock velocity (V_{sr}) ranges of 1421–1586 m s^{-1} and 767–1003 m s^{-1}, respectively (Table 1). The cyan and magenta curves represent the *SH* transfer functions for the same ground models by assuming a constant V_{sr} of 1500 and 2500 m s^{-1}, respectively. These values correspond to average V_{sr} proposed by Cushing *et al.* (2020) at an outcropping rock site, seated on the same geologic formation (upper Cretaceous limestones) as that of R02 and located about 2.6 km to the southeast of Array A, at 200 m and 400 m depths, respectively(Cushing *et al.* 2020). As there is no V_s profile available at the R02 reference site, using a range of V_{sr} values give us an idea about the sensitivity of the transfer functions with respect to the bedrock velocities. At A00, the amplification (Fig. 16e) observed at around 1.6 Hz could be attributed to the Airy phase of the fundamental mode of diffracted Love waves (Fig. 16c) and the amplification at 3.6 Hz could be attributed to the Airy phase of the first mode of diffracted Rayleigh waves (Fig. 16c) in retrograde motion (as seen in Fig. 15c). They also correspond to the first and second resonance peaks of 1-D vertically reverberating *SH*-wave transfer functions (Fig. 16e), with related amplifications depending on the impedance contrasts. At KES04 (next to the B04 station of Array B), we can also associate the amplifications within the same frequency bands with the Airy phase of Love and retrograde Rayleigh waves (Fig. 16d) and the 1-D site amplification (Fig. 16f). Interestingly, at these two array sites, the 1-D transfer functions are not able to explain the measured site amplification at frequencies in between the 1-D resonance peaks, amplification at those frequencies being caused by diffracted Love and Rayleigh surface waves (Figs 16a and b).

6 DISCUSSION

Local site conditions such as the geometry and properties of the subsurface materials can profoundly influence the amplitude, frequency content, and duration of a ground motion. In case of 1-D site conditions (i.e., flat geometry and horizontally layered soil), it is assumed that vertically propagating body waves passing through a horizontally layered soil profile are amplified on the surface at the resonance frequencies of the sedimentary layer. In a 2-D or 3-D environment (e.g. valleys, bedrock slope, changing geometry of the soft soil layers, topographical irregularities), body and surface waves diffracted at lateral heterogeneities propagate through the alluvium and can cause stronger and longer shaking than predicted by the 1-D assumption (among others, Kawase 1996; Cornou *et al.* 2003a,b; Stephenson *et al.* 2006; Bindi *et al.* 2009). Shallow, sediment-filled valleys are a common example of 2-D/3-D structures, where the interaction of the seismic wavefields with

the valley geometry and velocity contrasts at the boundaries cause the generation of additional surface waves at the valley edges (Bard & Bouchon 1980a,b, 1985). As a result, a complex amplification pattern is observed over a broad range of frequency, in relation with a mixture of body and surface waves of different kinds (Rayleigh / Love, fundamental and higher modes), rather than at well separated resonance frequencies linked to vertical reverberation of *S* waves. In order to better understand such phenomena, a characterization of the wavefield and determination of its association with the complexity of the underground structure is indispensable. The present work delves into this issue by analysing seismic records from two dense seismic arrays located on the shallow sedimentary valley of Koutavos-Argostoli in Cephalonia, Greece.

Our results clearly indicate that significant wave scattering takes place at the valley above its fundamental resonance frequency (∼1.5 Hz). We observe that various signal time windows throughout the duration of the event are most often complex mixtures of different types of waves. Diffracted waves also dominate the most energetic part of the signal in the earlier time windows that are classically considered to be composed of direct body waves. Exclusion of results associated to direct wave arrivals (event's backazimuth ±20å direction) showed that the wavefields are dominated by diffracted surface waves. Located relatively close to the southwestern edge of the valley on a relatively deeper soil column, Array A showed the presence of diffracted waves, arriving primarily from the southwest direction (N 210° ± 30°). At Array B, they arrive mainly from the nearby northeast edge (N 90° ± 30°) of the valley. Both arrays showed the presence of diffracted wave trains from the opposite edges as well. Diffracted waves dominated by Love waves also impinge the arrays, especially Array B, below the fundamental resonance frequency (<1.5 Hz) from the N 30°–N 90° direction. This probably manifests the influence of other regional low-frequency scatterers outside the valley (such as, possibly large-scale surface topography). However, this is just a hypothesis.

For both arrays, between 1 and 3 Hz, dispersion curve is mainly dominated by the fundamental mode of Love waves. The first and second higher modes of Love waves control the wavefield between 4 and 5 Hz and between 6 and 7 Hz, respectively. Between 3 and 4 Hz, the first harmonic mode of Rayleigh wave with retrograde particle motion, and between 5 and 6 Hz, the second higher mode of Rayleigh wave with prograde motion are relatively more energetic. These observations have also been confirmed by the theoretical phase velocities and ellipticities calculated from the inverted velocity models. It is to be noted that the fundamental mode Rayleigh wave is often thought to propagate in retrograde motion. We mainly observed it to be the opposite in our analysis. Actually, in case of a strong velocity contrast in the substructure, the ellipticity of the fundamental mode of Rayleigh waves will have a singular peak at the resonance frequency and a singular trough at a higher frequency. The particle motion changes and becomes prograde between these peak and trough frequencies. A number of recent studies (see Malischewsky *et al.* 2008 for a review) have also observed prograde motion for fundamental mode Rayleigh waves, especially in sedimentary basin environments.

Imtiaz (2015) showed that at both arrays, more than 80 per cent of the mean identified surface wave energy (Love + Rayleigh) corresponds to the diffracted waves while only around 20 per cent to the direct waves. We observed that at lower frequencies (1–3 Hz), diffracted Love and Rayleigh waves carried up to 60 and 20 per cent of the total energy, respectively. At higher frequencies, up to 40 per cent of the energy was carried by diffracted Love and Rayleigh waves each, where Rayleigh waves dominate over relatively narrow bands of frequency (e.g. 3–4 Hz and 5–6 Hz). These observations could be validated by the velocity structures beneath the arrays retrieved from geophysical measurements. The frequencies at which Airy phases appear on the theoretical group velocity curves, calculated from the velocity models, are in good agreement with the estimated peak energies of Love and Rayleigh waves.

We evaluated the site response in terms of SSR at two stations at the array locations and observed complex amplifications at different frequencies, which also demonstrates an excellent consistency with the identified surface wave types. For instance, the band of amplification at 1.6 ± 0.6 Hz could be associated with diffracted fundamental mode Love waves and at 3.6 ± 0.6 Hz with the first higher mode of retrograde Rayleigh waves. The peaks of estimated surface wave energy, Airy phases and amplification seem to be well-aligned, indicating an obvious correlation among these physical phenomena, in addition to *S*-wave amplification. The first resonance peak frequency of the theoretical 1-D transfer function is consistent with the corresponding peak on the amplification estimates, which confirms the 1-D resonance effect due to *SH*-wave (or Love wave) propagation. The second peak of the 1-D site response is slightly shifted compared to the observed second amplification peak, which may be simply understood as influenced by the Rayleigh waves. However, the *SH* peaks only represent single points and do not explain the observed amplification in between the 1-D resonance frequencies, which demonstrate the insufficiency of 1-D analysis in capturing the response of this site. It also highlights the contribution of surface waves in amplification in between the resonance frequency peaks. Such influence of locally generated surface waves on the site amplification over a wide frequency range was also observed by some previous studies (Cornou & Bard 2003; Bindi *et al.* 2009; Maufroy *et al.* 2015).

One concern of the study might be the fact that, at lower frequencies, a part of our results falls below the array resolution limit, especially in case of Array B. With reference to existing literature, it could be argued that the experimental resolution limit of an array could be wider than the theoretical one, especially when a high resolution technique like MUSIQUE is involved. The irregular shape of Array B obviously imposes some restriction on its resolution capacity. However, MUSIQUE results from both arrays seem to be in very satisfactory agreement with the theoretical dispersion curves obtained from the inverted velocity model. If the arrays were not able to resolve close wavenumbers, then we may have observed a bias to lower slowness estimation for all the modes. However, the backazimuth estimate is much less sensitive to the array resolution than the slowness. Moreover, results from Array B are also consistent with those from Array A. Therefore, we conclude that MUSIQUE outperformed the constraints posed by the array geometry.

One limitation of this study may arise from the prior assumption that only one particular wave, propagating from a certain direction with a certain apparent velocity, will dominate the wavefield in a single time–frequency window. When different waves carrying almost equal energy contribute to the wavefield, such a hypothesis may cause a bias in the results. This issue was addressed by Imtiaz (2015) by performing another set of analyses considering the dominance of two sources. In that case, MUSIQUE is unable to discriminate between Love and Rayleigh waves. The results were observed to be in agreement with the single-source hypothesis, confirming the principal directions of diffraction for both arrays. It is also to be noted that MUSIQUE is unable to separate *SH* waves from

Love waves. However, as the *SH* waves impinge almost vertically with a high apparent velocity (close to infinity), it is less likely that they have been misidentified as Love waves in our analysis.

7 CONCLUSION

This article presents results from the analysis of two dense seismic arrays and explored the wavefield characteristics generated by a set of local and regional earthquakes in the valley of Koutavos-Argostoli. The MUSIQUE algorithm was applied in order to extract the apparent propagation parameters (slowness and backazimuth) of the dominant waves crossing the arrays and to characterize the presence of surface waves as Love, prograde and retrograde Rayleigh waves. The results clearly indicate significant scattering, corresponding to probably 2-D or 3-D effects from the nearest valley edges, beyond the fundamental frequency (∼1.5 Hz) of the valley. The arrays are located close to the southwest and northeast edges of the valley, and diffracted waves arrive primarily from the respective directions (N 210° ± 30° and N 90° ± 30°). It appears that due to the relatively smaller width of the valley, both arrays capture the diffraction not only from the nearest but also from the farthest borders. Hence, we can conclude that the basin geometry is playing a prominent role in constraining the scattering of waves. On average, about 40–60 PER CENT of the total seismogram energy is carried by diffracted Love waves and 20–40 PER CENT by Rayleigh waves. While Love waves dominate around the fundamental resonance frequency of the valley (1–3 Hz), Rayleigh waves dominate over relatively narrow bands of higher frequencies (e.g. 3–4 Hz and 5–6 Hz). The estimated site amplifications at the two arrays demonstrate two distinct frequency bands of amplification at approximately 1.6 ± 0.6 Hz and 3.6 ± 0.6 Hz, which are in excellent agreement with the Airy phases associated with fundamental mode of Love and first higher mode of retrograde Rayleigh waves, respectively. These observations could also be validated by the velocity structures beneath the arrays, retrieved from active and passive geophysical measurements. The frequencies at which Airy phases appear on the theoretical group velocity curves are consistent with the estimated peak energies of Love and Rayleigh waves. Although the peak resonance frequencies of 1-D transfer functions are somewhat aligned with the Airy phases, they do not fully represent the broad range of observed spectral amplification. Once again, it confirms the influence of surface waves on the deviation from 1-D site effects. The outcomes of this research work outline the significance of analysing dense seismic arrays in order to better understand the contribution of edge-diffracted surface waves and the site amplification influenced by 2-D/3-D effects at small and shallow alluvium valleys like Argostoli. The wavefield characterization performed in this study can play a very important role in defining geometrical parameters of the site for developing a 3-D geological model. Such an analysis can be of particular interest in understanding the ability of 3-D ground motion models to capture the complex site effects. Comparison between the variability from the observed ground motions at dense arrays and the synthetics produced from numerical simulations of 3-D wave propagation could also help to evaluate to what extent these simulations can reproduce the statistical properties of 2-D/3-D site effects. Moreover, the Argostoli site can be of significant interest to the earthquake engineering community. A wealth of high-quality data is available at this site from the seismic instrumentation deployed under several projects following NERA. Being located in an active tectonic environment and very close to the Cephalonia Transform Fault, Argostli has been subjected to a high level of near-field ground motion during a number of major past earthquakes. Hence, understanding the complex wavefield characteristics from such a site would definitely contribute in performing reliable seismic hazard assessment.

DATA AND RESOURCES

The data used in the present work are open and can be obtained on the data repository of the European Integrated Data Archive (FDSN 4C 2011) and are presented in Theodoulidis *et al.* (2018).

ACKNOWLEDGEMENTS

The authors would like to thank all EU NERA (https://cordis.europa.eu/project/rcn/96282 en.html) partner institutions who participated in the seismological experiment (Institut des Sciences de la Terre [ISTERRE], Grenoble, France; Instituto Nationale di Geofisicale Vulcanologia [INGV], Rome, Italy; GeoForschungsZentrum [GFZ], Potsdam, Germany; Institute of Engineering Seismology and Earthquake Engineering [EPPO-ITSAK], Thessaloniki, Greece). Special thanks goes to Nikos Theodulidis (ITSAK), Giovanna Cultrera (INGV), Tobias Boxberger (GFZ), Tommy Andreou (Technological Educational Institute of Ionian Islands, Argostoli, Greece and ITSAK) and Fabrice Hollender (Commissariat à l'Énergie atomique et aux Énergies [CEA], France). Array A was deployed by the Institut des Sciences de la Terre (ISTerre), Grenoble, France. Seismological data of Array A have been acquired by using the stations from SISMOB/RESIF (INSU/CNRS) mobile pool, which is a member of French Seismologic and Geodetic Network (RESIF - Réseau Sismologique et Géodésique Français). RESIF is a national Research Infrastructure recognized as such by the French Ministry of higher education and research. It is additionally supported by a public grant overseen by the French national research agency (ANR) as part of the "*Investissements d'Avenir*" program (reference: ANR-11-EQPX-0040) and the French Ministry of Ecology, Sustainable Development and Energy. Array B was deployed by the German Research Centre for Geosciences (GFZ). Data of Array B have been acquired by using the stations from the Geophysical Instrument Pool of Potsdam (GIPP) of GFZ. The updated geological map and the 2-D cross-section of the site have been developed under the framework of SINAPS@ project (http://www.institut-seism.fr/projets/sinaps/). The authors would like to take this opportunity to thank the editors of the GJI and the esteemed reviewers Prof. Hiroshi Kawase and Prof. Brendon Bradley for their contributions in the review process of the papere authors greatly appreciate their constructive suggestions and inspiring comments, which have helped to improve the manuscript.

REFERENCES

Almendros, J. *et al.*, 2000. A double seismic antenna experiment at Teide Volcano: existence of local seismicity and lack of evidences of volcanic tremors. *J. Volc. Geotherm. Res.,* **103,** 439–462.

Asten, M.W. & Henstridge, J.D., 1984. Array estimators and the use of microseisms for reconnaissance of sedimentary basins. *Geophysics,* **49,** 1828–1837.

Bard, P.-.Y. & Bouchon, M., 1980a. The seismic response of sediment-filled valleys. Part 1. The case of incident *SH* waves. *Bull. seism. Soc. Am.,* **70,** 1263–1286.

Bard, P.-.Y. & Bouchon, M., 1980b. The seismic response of sediment-filled valleys. Part 2. The case of incident *P* and *SV* waves. *Bull. seism. Soc. Am.,* **70,** 1921–1941.

Bard, P.-Y. & Bouchon, M., 1985. The two-dimensional resonance of sediment filled valleys. *Bull. seism. Soc. Am.,* **75,** 519–541.

Bear, L.K., Pavlis, G.L. & Bokelmann, G.H., 1999. Multi-wavelet analysis of three-component seismic arrays: application to measure effective anisotropy at Pinon Flats, California. *Bull. seism. Soc. Am.,* **89,** 693–705.

Bindi, D. *et al.*, 2009. Site amplifications observed in the Gubbio Basin, Central Italy: hints for lateral propagation effects. *Bull. geol. Soc. Am.,* **99,** 741–760.

Bokelmann, G.H.R. & Baisch, S., 1999. Nature of narrow-band signals at 2.083 Hz. *Bull. seism. Soc. Am.,* **89,** 156–164.

Bonnefoy-Claudet, S., Köhler, A., Cornou, C., Wathelet, M. & Bard, P.-Y., 2008. Effects of Love waves on microtremor H/V ratio. *Bull. seism. Soc. Am.,* **98,** 288–300.

Boxberger, T. *et al.*, 2014. Effect of the underground structure on the wavefield : the high-resolution experiment in Cephalonia Island (Greece), pp. 2–4, in *Second European Conference on Earthquake Engineering and Seismology (2ECEES),* Istanbul, Turkey.

Capon, J., 1969. High-resolution frequency-wavenumber spectrum analysis. *Proc. IEEE,* **57,** 1408–1418.

Caserta, A., Marra, A. & Bellucci, F., 1998. Strong diffraction effects at the edge of the Colfiorito, Central Italy, basin, in *Second Int. Symp. Eff. Surf. Geol. Seism. Motion,* Balkema, Yokohama, pp. 435–440.

Casto, D.W., Calderón-Macías, C., Luke, B. & Kaufmann, R., 2010. Improving MASW results for a site with shallow bedrock through the use of higher-mode data, in *Proc. GeoFlorida 2010,* West Palm Beach, Florida, pp. 1360–1368.

Chávez-García, F.J., Stephenson, W.R. & Rodríguez, M., 1999. Lateral propagation effects observed at Parkway, New Zealand. A case of history to compare 1D versus 2D site effects. *Bull. seism. Soc. Am.,* **89,** 718–732.

Cornou, C. & Bard, P.-Y., 2003. Site-to-bedrock over 1D transfer function ratio: An indicator of the proportion of edge-generated surface waves? *Geophys. Res. Lett.,* **30,** 1453. doi:10.1029/2002GL016593

Cornou, C., Bard, P.-Y. & Dietrich, M., 2003a. Contribution of dense array analysis to the identification and quantification of basin-edge induced waves, part I: methodology. *Bull. seism. Soc. Am.,* **93,** 2604–2623.

Cornou, C., Bard, P.-Y. & Dietrich, M., 2003b. Contribution of dense array analysis to basin-edge-induced waves identification and quantification, part II: application to Grenoble basin, French Alps. *Bull. seism. Soc. Am.,* **93,** 2624–2648.

Cornou, C., Ohrnberger , M., Boore, D.M., Kudo, K.M. & Bard, P.-Y., 2006. Using ambient noise array techniques for site characterisation: results from an international benchmark, in *Proc. 3rd Int. Symp. Eff. Surf. Geol. Seism. Motion,* Grenoble, France.

Cultrera, G. *et al.*, 2014. The Argostoli (Cephalonia, Greece) experiment, in *Proc. Second Eur. Conf. Earthq. Eng. Seismol. (2ECEES),* Istanbul, Turkey.

Cushing, E.M. *et al.*, 2016. Close to the lair of Odysseus Cyclops : the SINAPS@ postseismic campaign and accelerometric network installation on Kefalonia island – site effectcharacterizationexperiment, in *Proc. 7th INQUA Paleoseismology, Act. Tectonics Archeoseismology, Crestone, Color. USA,* eds. McCalpin, J. & Gruetzner, C.

Cushing, E.M. *et al.*, 2020. Building a three dimensional model of the active Plio-Quaternary basin of Argostoli (Cephalonia Island, Greece): an integrated geophysical and geological approach. *Eng. Geol.,* **265,** 105441, doi:10.1016/J.ENGGEO.2019.105441

Dainty, A.M. & Toksöz, M.N., 1990. Array analysis of seismic scattering. *Bull. seism. Soc. Am.,* **80,** 2242–2260.

Fäh, D., Kind, F. & Giardini, D., 2003. Inversion of local *S*-wave velocity structures from average H/V ratios, and their use for the estimation of site-effects. *J. Seismol.,* **7,** 449–467.

FDSN 4C (2011). FDSN Network 4C (2011-2014): NERA-JRA1-A. NERA JRA1 Argostoli basin experiment. Operated by the Observatoire de Grenoble. Available at: http://www.fdsn.org/networks/detail/4C_2011/ and http://orfeus-eu.org/stationbook/networks/4C/2011/.

Field, E.H., 1996. Spectral amplification in a sediment-filled valley exhibiting clear basin-edge-induced waves. *Bull. seism. Soc. Am.,* **86,** 991–1005.

Gaffet, S., Larroque, C., Deschamps, A. & Tressols, F., 1998. A dense array experiment for the observation of waveform perturbations. *Soil Dyn. Earthq. Eng.,* **17,** 475–484.

Goldstein, P. & Archuleta, R.J., 1987. Array analysis of seismic signals. *Geophys. Res. Lett.,* **I4,** 13–16.

Goldstein, P. & Archuleta, R.J., 1991. Deterministic frequency-wavenumber methods and direct measurements of rupture propagation during earthquakes using a dense array: Data analysis. *J. geophys. Res.,* **96,** 6187–6198.

Gouédard, P., Cornou, C. & Roux, P., 2008. Phase–velocity dispersion curves and small-scale geophysics using noise correlation slantstack technique. *Geophys. J. Int.,* **172,** 971–981.

Hobiger, M., 2011. *Polarization of Surface Waves : Characterization, Inversion and Application to Seismic Hazard Assessment,* Université de Grenoble.

Hobiger, M., Bihan, N.Le, Cornou, C. & Bard, P.-Y., 2012. Multicomponent signal processing for Rayleigh wave ellipticity estimation application to seismic hazard assessment. *IEEE Signal Process. Mag.,* **29,** 29–39.

Hobiger, M., Cornou, C., Bard, P.-Y. & Bihan, N.Le., 2011. MUSIQUE: a quaternion-based array processing technique for surface wave polarization analysis, in *IEEE Signal Process. Work. Stat. Signal Process*, doi:10.1109/SSP.2011.5967770.

Hobiger, M., Cornou, C., Bard, P.-Y., Bihan, N.Le & Imperatori, W., 2016. Analysis of seismic waves crossing the Santa Clara Valley using the three-component MUSIQUE array algorithm. *Geophys. J. Int.,* **207,** 439–456.

Hobiger, M. *et al.*, 2013. Ground structure imaging by inversions of Rayleigh wave ellipticity: sensitivity analysis and application to European strong-motion sites. *Geophys. J. Int.,* **192,** 207–229.

Hollender, F. *et al.*, 2015. Close to the lair of Odysseus Cyclops : the SINAPS@ postseismic campaign and accelerometric network installation on Kefalonia Island, in *9th Colloq. Natl. AFPS*, Marne-La-Vallée, France,p. 13.

Imtiaz, A., 2015, Seismic wave field, spatial variability and coherency of ground motion over short distances : near source and alluvial valley effects, *PhD thesis*, Université Grenoble Alpes, France,.

Imtiaz, A., Cornou, C. & Bard, P.-Y., 2018a. Sensitivity of ground motion coherency to the choice of time windows from a dense seismic array in Argostoli, Greece. *Bull. Earthq. Eng.,* **16,** 3605–3625,.

Imtiaz, A., Cornou, C., Bard, P.-Y. & Zerva, A., 2018b. Effects of site geometry on short-distance spatial coherency in Argostoli, Greece. *Bull. Earthq. Eng.,* **16,** 1801–1827,.

James, D.E., 1989., in *Geophysics. Encyclopedia of Earth Science,* Springer.

Jurkevics, A., 1988. Polarization analysis of three component array data. *Bull. seism. Soc. Am.,* **78,** 1725–1743.

Kawase, H., 1996. The cause of the damage belt in Kobe: 'the basin-edge effect', constructive interference of the direct *S*-wave with the basin-induced diffracted/Rayleigh waves. *Seismol. Res. Lett.,* **67,** 25–34.

Kawase, H., Matsushima, S., Satoh, T. & Sánchez-Sesma, F.J., 2015. Applicability of theoretical horizontal-to-vertical ratio of microtremors based on the diffuse field concept to previously observed data. *Bull. seism. Soc. Am.,* **105,** 3092–3103.

Krim, H. & Viberg, M., 1996. Two decades of array signal processing<p>research: the parametric approach. *IEEE Signal Process. Mag.,* **13,** 67–94.

Kuwahara, Y., Ito, H., Kawakatsu, H., Ohminato, T. & Kiguchi, T., 1997. Crustal heterogeneity as inferred from seismic coda wave decomposition by small-aperture array observation. *Phys. Earth planet. Inter.,* **104,** 247–256.

Lacoss, R.T., Kelly, E.J. & Toksöz, M.N., 1969. Estimation of seismic noise structure using arrays. *Geophysics,* **34,** 21–38.

Lekkas, E., Danamos, G. & Mavrikas, G., 2001. Geological structure and evolution of Cefallonia and Ithaki Islands. *Bull. Geol. Soc. Greece,* **34,** 11–17.

Lontsi, A.M., Sánchez-Sesma, F.J., Molina-Villegas, J.C., Ohrnberger, M. & Krüger, F., 2015. Full microtremor H/V(z, f) inversion for shallow subsurface characterization. *Geophys. J. Int.,* **202,** 298–312.

Louvari, E., Kiratzi, A. & Papazachos, B.C., 1999. The Cephalonia Transform fault and its extension to western Lefkada Island (Greece). *Tectonophysics,* **308,** 223–236.

Lunedei, E. & Albarello, D., 2010. Theoretical HVSR curves from full wavefield modelling of ambient vibrations in a weakly dissipative layered Earth. *Geophys. J. Int.,* **181,** 1093–1108.

Malischewsky, P.G., Scherbaum, F., Lomnitz, C., Tuan, T.T., Wuttke, F. & Shamir, G., 2008. The domain of existence of prograde Rayleigh-wave particle motion for simple models. *Wave Motion,* **45,** 556–564.

Manea, E.F., Michel, C., Hobiger, M., Fäh, D., Cioflan, C.O. & Radulian, M., 2017. Analysis of the seismic wavefield in the Moesian Platform (Bucharest area) for hazard assessment purposes. *Geophys. J. Int.,* **210,** 1609–1622.

Maranò, S., Hobiger, M. & Fäh, D., 2017. Retrieval of Rayleigh wave ellipticity from ambient vibration recordings. *Geophys. J. Int.,* **209,** 334–352.

Maranò, S., Reller, C., Loeliger, H.-A. & Fäh, D., 2012. Seismic waves estimation and wavefield decomposition: application to ambient vibrations. *Geophys. J. Int.,* **191,** 175–188.

Maufroy, E. *et al.*, 2015. Earthquake ground motion in the Mygdonian Basin, Greece: the E2VP verification and validation of 3D numerical simulation up to 4 Hz. *Bull. seism. Soc. Am.,* **105,** 1398–1418.

Miron, S., Bihan, N.Le & Mars, J., 2005. High resolution vector-sensor array processing using quaternions, in *IEEE/SP 13th Work. Stat. Signal Process*, Bordeaux, France, pp. 918–923.

Miron, S., Bihan, N.Le & Mars, J., 2006. Quaternion-MUSIC for vector-sensor array processing. *IEEE Trans. Signal Process,* **54,** 1218–1229.

Moczo, P. & Bard, P.-Y., 1993. Wave diffraction, amplification and differential motion near strong lateral discontinuities. *Bull. seism. Soc. Am.,* **83,** 85–106.

Pichon, X.Le, Chamot-Rooke, N., Lallemant, S., Noomen, R. & Veis, G., 1995. Geodetic determination of the kinematics of Central Greece with respect to Europe: implications for Eastern Mediterranean tectonics. *J. geophys. Res.,* **100,** 12675–12 690.

Poggi, V. & Fäh, D., 2010. Estimating Rayleigh wave particle motion from three-component array analysis of ambient vibrations. *Geophys. J. Int.,* **180,** 251–267.

Protopapa, E., Papastamatiou, D.M. & Gazetas, G., 1998. The Ionianet accelerometer array : early results and analysis, in *Proc. 11th Eur. Conf. Earthq. Eng.*, Balkema, Rotterdam, pp. 1–8.

Roullé, A. & Chávez García, F.J., 2005. Comparison of three methods to study the wavefield in the valley of Mexico using data from dense arrays. *Rev. Ing. Sísmica,* **73,** 1–25 .

Rovelli, A., Scognamiglio, L., Marra, F. & Caserta, A., 2001. Edge-diffracted 1-sec surface waves observed in a small-size intramountain basin (Colfiorito, central Italy). *Bull. seism. Soc. Am.,* **91,** 1851–1866.

Sánchez-Sesma, F.J. *et al.*, 2011. A theory for microtremor H/V spectral ratio: application for a layered medium, *Geophys. J. Int.,* **186,** 221–225.

Scandella, L. & Paolucci, R., 2010. Earthquake induced ground strains in the presence of strong lateral soil heterogeneities. *Bull. Earthq. Eng.,* **8,** 1527–1546.

Schmidt, R.O., 1981. *A Signal Subspace Approach to Multiple Emitter Location and Spectral Estimation,* Stanford University.

Schmidt, R.O., 1986. Multiple emitter location and signal parameter estimation. *IEEE Trans. Antennas Propag.,* **34,** 276–280.

Stephenson, W.J., Frankel, A.D., Odum, J.K., Williams, R.A. & Pratt, T.L., 2006. Toward resolving an earthquake ground motion mystery in west Seattle, Washington State: shallow seismic focusing may cause anomalous chimney damage. *Geophys. Res. Lett.,* **33**. doi:10.1029/2005GL025037

Tchawe, F.N., Froment, B., Campillo, M. & Margerin, L., 2020. On the use of the coda of seismic noise autocorrelations to compute H/V spectral ratios. *Geophys. J. Int.,* **220,** 1956–1964.

Theodoulidis, N. *et al.*, 2018. Basin effects on ground motion: the case of a high-resolution experiment in Cephalonia (Greece). *Bull. Earthq. Eng.,* **16,** 1–32,.

Wagner, G.S. & Owens, T.J., 1993. Broadband bearing time records of three component seismic array data and their application to the study of local earthquake coda. *Geophys. Res. Lett.,* **20,** 1823–1826.

Ward, J.P., 1997. *Quaternions and Cayley Numbers: Algebra and Applications,* Kluwer Academic Publishers.

Wathelet, M., Jongmans Ohrnberger, M.D. & Bonnefoy-Claudet, S., 2008. Array performances for ambient vibrations on a shallow structure and consequences over Vs inversion. *J. Seismol.,* **12,** 1–19.

Zerva, A. & Zhang, O., 1996. Estimation of signal characteristics in seismic ground motions. *Probabilistic Eng. Mech.,* **11,** 229–242.